Distinctive optoelectronic properties of nanostructured MoS_2 bilayers

Vladan Mlinar*

Research Institute for Advanced Materials Design, Providence, Rhode Island 02906, USA

(Received 29 December 2018; revised manuscript received 24 July 2019; published 8 August 2019)

We theoretically investigate the electronic and optical properties of nanostructured MoS_2 bilayers, consisting of vertically stacked monolayer (ML) of pristine MoS_2 and ML of periodic triangular nanoplatelets or holes. Our calculations reveal that the interplay between edge atoms in periodic nanostructures, size of nanostructures, and distances between them, control the appearance and size of the band gaps, and optical response, including the number and intensity of peaks; the nanostructured bilayers with periodic nanoplatelets in particular exhibit rich optical properties. Specifically, we find the electronic states, originating from the atoms of the ML with either periodic nanoplatelets or holes, get embedded between electronic states of pristine MoS_2 ML, but now with red- and blueshifted valence and conduction bands, respectively. For a ML with periodic nanoplatelets, electronic states originate primarily from p orbitals of S atoms, and for a ML with periodic holes, they originate from d orbitals of Mo atoms. The electronic structure is accessed through the self-consistent tight-binding (SCTB) method, which is the extension of our tested parametrized TB model that includes nonorthogonal sp^3d^5 orbitals and spin-orbit coupling. We systematically examine the parameters in our SCTB to avoid possible distortion of electronic states, ensuring high quality of our predictions.

DOI: 10.1103/PhysRevB.100.085411

I. INTRODUCTION

Semiconducting transition metal dichalcogenides (TMDs), such as MoS_2, WS_2, $MoSe_2$, or WSe_2, have reportedly exhibited distinct, layer dependent properties, which have qualified them to serve as platform to uncover intriguing two dimensional electronic physics [1–8]. Revealed features also inspired quest for appropriate applications, including solar cells, [5,9] field effect transistors [10–12], or valleytronics [13–15], to name just a few examples.

Further modifications of specific properties of pristine TMDs, where our primary focus is on the electronic and optical properties, have been based on altering certain aspects of the structure. Attention of numerous theoretical and experimental investigations has been directed toward investigations of nanostructured TMDs, such as nanowires, [16–21] and nanoplateletes [22–24], vertically and laterally stacked heterostructures of different TMDs [25–31], defects in a single monolayer (ML) of pristine TMDs [32,33], and controllable effects of external electric and magnetic fields [14,34–41].

For example, for nanostructured MoS_2, presence of edges was shown to lead to the occurrence of electronic states in the band gap [23,24]. On the one hand, this fact implies potential applications as thermoelectric materials or as catalysts [23]. On the other, it makes the existence of band gap, as one of the advantages of pristine MoS_2 over graphene, lost for the finite-sized MoS_2. Interestingly, by engineering the edges of MoS_2 nanowires, i.e., for a certain combination of the edge atoms that influence nonbonding S-atom p orbitals and Mo atom d orbitals, one could open and tune a band gap [24].

Next, it was experimentally demonstrated that different TMDs can be stacked vertically ML by ML, forming vertically stacked TMD heterostructures [25,27,29,42]. The choice of constituent components and the number of MLs of given TMD in a heterostructure dictates the structural stability and the electronic properties of these systems [25–28,43–45]. For example, intrinsic strain in $MoS_2/MoSe_2$ or $MoSe_2/MoTe_2$ heterostructures was induced by the lattice mismatch between constituent TMDs, and was theoretically demonstrated to influence the structural stability [43]. Furthermore, it was suggested that bilayer TMD heterostructures, in particular MoS_2/WS_2 could be used in solar cells because of their type II alignment where MoS_2 behaves as acceptor, and WS_2 as donor [9]. A recent experimental report introduced MoS_2-WS_2 hybrid structures that combined both vertical and in-plane heterostructures [46].

Point and line defects in a ML of TMDs were shown to modify the electronic, optical, and transport properties [32,33,47]. For example, Mo (or W) point defects in 1ML of MoS_2 (or WS_2) introduce midgap states, which are spatial localized on the defect, behaving similarly to resonant scatterers in graphene [32]. Also, defects in a 1ML of a TMD could lead to the enhanced nonradiative recombination [48], and should be controllable for potential application in optoelectronic devices [49].

Here, we explore an alternative avenue in tuning the electronic and optical properties of TMD-based nanomaterials; we introduce a nanostructured TMD-based bilayer system. It consists of a ML of a pristine TMD, and a two-dimensional (2D) array of a few atom TMD-based nanostructures in the second ML, where the MLs interact through van der Waals (vdW) force. We cast MoS_2 as a representative of TMDs, given that pristine and nanostructured MoS_2 has been widely studied both experimentally and theoretically [22–24,50]. For periodic nanostructures, we consider triangular nanoplatelets and holes.

*vladan.mlinar@riamd.org

We find that the interplay between edge atoms in periodic nanoplatelets or holes, their sizes, and distances between them, control the appearance and size of the band gaps, and optical response. Our calculations reveal the electronic states, originating from the atoms of the ML with either periodic nanoplatelets or holes, get embedded between electronic states of pristine MoS_2 ML, but now with red- and blueshifted valence and conduction bands, respectively. For a ML with periodic nanoplatelets, electronic states originate primarily from p orbitals of S atoms, and for a ML with periodic holes, they originate from d orbitals of Mo atoms. Whereas the nanostructured bilayers with periodic holes exhibit rather poor optical response, the bilayers with periodic nanoplatelets exhibit rich optical properties, characterized by the number and intensity of peaks.

Given rapid progress in fabrication techniques of TMD-based systems, such as reduced dimensionality nanostructures [16,17,22,25,26,50,51], vdW heterostructures [46,51–53], and ML alloys such as MoS_2-WS_2 or $MoSe_2$-WSe_2 [46], it is reasonable to expect experimental realization and characterization of arbitrary TMD-based nanostructured system with control at subnanometer scales, see, e.g., Refs. [21,25,46,50,54,55]. In this light, our theoretical findings could motivate further experimental and theoretical investigations of the nanostructured bilayers and inspire potential applications in, e.g., high-performance optoelectronic devices [5,46,56], including their targeted design [57].

The electronic structure of our nanostructured MoS_2 bilayer systems is resolved within a self-consistent tight binding (SCTB) model. We advance our parametrized tight binding (TB) model with nonorthogonal sp^3d^5 orbitals and spin-orbit coupling (SOC) [24,27,41] to include a self-consistency loop [24,58,59]. In such a way, we prevent possible occurrences of an improper charge redistribution and nonphysically large charge transfers at surface of a few-atom nanostructure in the second ML of our nanostructured MoS_2 bilayer system. We systematically test parameters in our SCTB, ensuring high quality of our predictions.

We also note that our parametrized TB model (without SC loop) has been previously tested; its predictions of the electronic structure of pristine 1ML, 2ML, and bulk MoS_2 [24], nanostructured MoS_2 [24], and vertically stacked MoS_2/WS_2 heterostructures [27], exhibited good agreement with findings extracted from density functional theory (DFT), *GW*, and experiment.

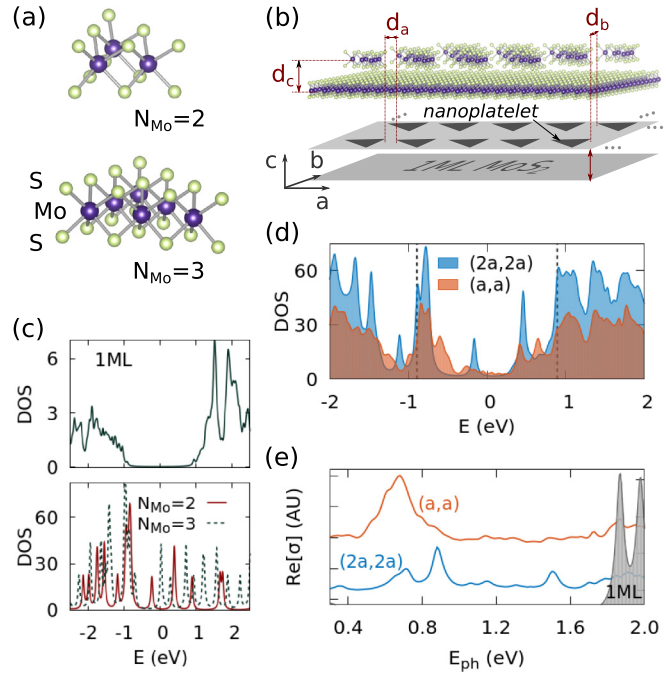

FIG. 1. (a) Structure of MoS_2 nanoplatelet; top panel depicts a Mo_3S_{12} nanoplatelet with $N_{Mo} = 2$, and bottom panel Mo_6S_{20} with $N_{Mo} = 3$; (b) periodic nanostructured MoS_2 bilayer system, consisting of MoS_2 ML and a 2D array of MoS_2 nanoplatelets in the second layer. Nanoplatelets are separated by d_a and d_b, and by d_c from bottom MoS_2 ML. Typically $d_c = c/2$ (see also the text and Fig. 4). Atomistic structure is shown in the top panel and the geometric sketch at the bottom; (c) calculated DOS for pristine 1ML MoS_2 (top), and Mo_3S_{12} with $N_{Mo} = 2$, and Mo_6S_{20} with $N_{Mo} = 3$ nanoplatelets (bottom); (d) calculated DOS for our nanostructured bilayers with $(d_a, d_b) = (2a,2a)$ (blue shaded region) and $(d_a, d_b) = (a,a)$ (orange shaded region). The vertical dashed lines at -0.895 and 0.890 eV correspond to the valence band maximum and conduction band minimum of pristine 1ML MoS_2, respectively; (e) calculated real part of optical conductivity, $\mathrm{Re}[\sigma]$, for our MoS_2-based systems with $(d_a, d_b) = (2a,2a)$ (blue line) and $(d_a, d_b) = (a,a)$ (orange line). Gray shaded region shows $\mathrm{Re}[\sigma]$ for pristine 1ML MoS_2. Please note scale of $\mathrm{Re}[\sigma]$ for 1ML MoS_2 is given on the right ordinate and differs from those of nanostructured bilayer systems with (0,0) and (a,a).

II. METHOD

A. Model structure

Figures 1(a) and 1(b) show the structure of the nanostructured MoS_2 bilayer system analyzed in this work. Our model systems consist of a bottom ML of pristine MoS_2, and a 2D array of few-atom MoS_2 nanoplatelets in the top layer. The top layer is bounded to the MoS_2 ML by weak vdW forces.

We focus on triangularly shaped nanoplatelets [Fig. 1(a)] because this shape has been found in experimental studies [25,26,46,50,54,60]. For example, Cain *et al.* demonstrated an on-demand, temperature tunable synthesis of vertically stacked, in-plane and hybrid triangular heterostructures, and alloying within a ML [46]. Gong *et al.* reported synthesis of vertical and in-plane triangular heterostructures consisting of MoS_2 and WS_2 MLs [25] and $MoSe_2$ and WSe_2 MLs [26]. The reader is referred to Refs. [21,25,46,50,54,55] for additional details on structural characterization of MoS_2 (and other TMD-based) nanoplatelets.

By combining experimentally extracted STM images and DFT calculations, Lauritsen *et al.* found that the edge structure of triangular MoS_2 nanoplatelets consist of Mo edges fully covered with S atoms [50]. Namely, a triangular shape of MoS_2 nanoplatelets indicates only one of two low index edge terminations of an MoS_2 hexagon, either the $(10\bar{1}0)$ Mo edges or the $(\bar{1}010)$ S edges. Experimental data coupled with DFT calculations determined that $(10\bar{1}0)$ Mo edges fully covered with S terminate MoS_2 nanoplatelets [22,23,50]. For completeness, detailed and more general discussion regarding trends in surface composition can be found in Ref. [61].

Triangular TMD nanoplatelets have been employed in different theoretical studies [22,23,27,54]. For example, triangular TMD-based nanoplatelets were used for development and testing of a predictive growth model that involved thermodynamic and kinetic factors, including the criteria for vertical stacking [54]. Also, Li and Galli calculated the electronic properties of homogeneous MoS_2 triangular nanoplatelets [model nanoplatelets identical to ours in Fig. 1(a)], and nanowires based on triangular nanoplatelets [23].

Our model nanoplatelets are characterized by their size, i.e., by the number of Mo and S atoms in the nanoplatelet, and the number of Mo atoms at the edge, N_{Mo}. For example, the top nanoplatelet in Fig. 1(a) is defined by Mo_3S_{12} and $N_{Mo} = 2$, and the bottom nanoplatelet by Mo_6S_{20} and $N_{Mo} = 3$. In this work, we consider nanoplatelets ranging from $N_{Mo} = 2$ to $N_{Mo} = 4$.

Experimentally, triangular nanoplatelets as small as $N_{Mo} = 4$ were observed. Combination of experimental data and DFT calculations identified the nanoplatelets with the edge configuration with 100% S coverage to be the most stable [50]. For smaller triangular nanoplatelets, $N_{Mo} < 4$, Lauritsen *et al.* reported experimentally plausible edge configurations, including also S concentrations at the edges of 50% and 75% [50]. In this work, we consider triangular nanoplatelets with edge configuration with 100% S coverage [e.g, as shown in Fig. 1(a)], but also discuss the influence of the reduced S concentration at the edges of 75% and 50% [see top panels in Fig. 5(a) and Ref. [50]].

Nanoplatelets in the array [top ML in Fig 1(b)] are separated by d_a and d_b in the **a** and **b** directions, respectively. We vary the distances between nanoplatelets in the array, and also the distance between top and bottom MLs, d_c. Here, we consider (d_a, d_b) varying from (a,a) to (4a,4a).

Within our study we also discuss the case where nanoplatelets and space between them in the top ML are replaced by holes and MoS_2, respectively. In a simple term, it is an "inverse" structure to our original structure, where, as a result, the top ML of the nanostructured bilayer consists of periodic triangular holes in MoS_2 matrix. For more details, see Fig. 7 and the corresponding discussion.

B. Our approach

The electronic structure of our nanostructured MoS_2 bilayer systems is resolved in the framework of a SCTB method. We introduce a self-consistency loop to our previously developed and tested parametrized TB model, with nonorthogonal sp^3d^5 orbitals and SOC [24,27].

By incorporating the self-consistency loop to our model, we avoid the risk of the appearance of nonphysically large or spurious charge transfers in the array of nanoplatelets in the top ML of our structure [cf. Fig. 1(b)]. This could cause the displacement of surface states and distorted density of states (DOS) [24,58,59]. We remind the reader that in *ab initio* calculations, the Hamiltonian is solved self-consistently, ensuring a quasicharge neutrality of each atom [58].

Converged eigenvalues and eigenvectors from our SCTB model are then used to calculate total DOS, density of states projected on atoms and/or orbitals of atoms (pDOS), and the real part of optical conductivity in dipole approximation, which gives us information about the optical response of the material [8,24,62–70].

Parametrized TB model. Our parametrized TB model *without* self-consistency has been already employed to describe the electronic and optical properties of pristine 1ML, 2ML, and bulk MoS_2, nanostructured MoS_2 [24], and vertically stacked MoS_2/WS_2 heterostructures. [27] Also, within our approach we established the role of external electric [27] and magnetic fields [41].

Detailed discussion regarding the implementation of our parametrized TB model can be found in Refs. [24,27,41]. Here, we provide a brief overview.

Interactions between atoms within a ML, S-S, Mo-S, Mo-Mo, are constrained to the nearest neighbor, and between MLs to the second nearest neighbor, sulfur atoms [24,27]. For each atom (Mo or S), SOC includes only intra-atomic states with nonzero angular momentum [24,71,72]. Our parametrized TB model, when applied to MoS_2 uses a set of ninety six parameters derived by Zahid *et al.* that includes the on-site energy terms, SOC, and energy and overlap integrals [24, 73–77].

*Self-consistency.*Within our parametrized TB method [24,27,41] and employed parametrization [74,76], the on-site energies were fixed and fitted to reproduce the band structure of 1ML, 2ML, and bulk MoS_2 [24,74]. In order to account for interatomic charge redistribution in our nanostructured MoS_2 bilayers [cf. Fig. 1(b)] and avoid occurrence of distorted DOS [24,58,59,78,79], we impose the local charge neutrality within self-consistency. Specifically, within our SCTB approach, on-site energies get shifted until the system reaches a stable equilibrium contingent on charges; for additional details see Refs. [24,58,59,80].

We are solving the following problem [81–84]:

$$\sum_{b',\beta}[H_{\mathrm{SCTB}}]^{b,b'}_{\alpha,\beta}(\mathbf{k})C_{\mathbf{k},n}(b',\beta) = \epsilon_n(\mathbf{k})\sum_{b',\beta} S^{b,b'}_{\alpha,\beta}(\mathbf{k})C_{\mathbf{k},n}(b',\beta), \tag{1}$$

where H_{SCTB} and S are SCTB Hamiltonian and overlap matrix, respectively. $\epsilon_n(\mathbf{k})$ are eigenvalues and $C_{\mathbf{k},n}$ the expansion coefficients for the eigenvectors of the band n. b (b') labels a basis atom, and α (β) orbital types on that atom.

The SCTB Hamiltonian is given by [81,82,84,85]

$$[H_{\mathrm{SCTB}}]^{b,b'}_{\alpha,\beta}(\mathbf{k}) = [H_{\mathrm{TB}}]^{b,b'}_{\alpha,\beta}(\mathbf{k}) + \tfrac{1}{2}U_{\mathrm{LCN}}\big[\big(Q^{\mathrm{Mull}}_b - Z^0_b\big) + \big(Q^{\mathrm{Mull}}_{b'} - Z^0_{b'}\big)\big]S^{b,b'}_{\alpha,\beta}, \tag{2}$$

where $[H_{\mathrm{TB}}]$ is the parametrized TB Hamiltonian, [24] Q^{Mull}_b is the Mulliken charge on the atom b, and Z^0_b is the targeted bulk value of the number of valence electrons in the atom b. We remind the reader that $Q^{\mathrm{Mull}}_b = \sum_\alpha \sum_{\mathbf{k},n}\{1/(\exp[k_BT(\epsilon_n(\mathbf{k}) - E_f)] + 1\}C^\dagger_{\mathbf{k},n}(b,\alpha)S(\mathbf{k})C_{\mathbf{k},n}(b,\alpha)$, where E_f is the Fermi energy, and k_BT is thermal smearing [85–87]. U_{LCN} is the local charge neutrality constant, where we adopt $U_{\mathrm{LCN}} = 8$ eV after testing different values (see below).

In the self-consistent loop, we solve Eq. (1), which depends on charges, to obtain eigenvalues and eigenvectors, and then calculate Mulliken charges using eigenvalues and

eigenvectors. For each and every atom b in the supercell, we impose the convergency criterion:

$$\left|\left(Q_b^{\mathrm{Mull}}\right)_{it=i+1} - \left(Q_b^{\mathrm{Mull}}\right)_{it=i}\right| < tol, \tag{3}$$

where we adopt $tol = 10^{-4}$ after testing different values of tol (see below).

An efficient convergence in our SCTB calculations is achieved through implementation of a modified Broyden's method introduced by Johnson [88]. Each self-consistency cycle contains information from all previous iterations [89], and is solved within the Srivistava's computational scheme [90].

Within our SCTB approach, we need to find appropriate values for parameters U_{LCN} and tol. U_{LCN} controls how rigorous is the constraint on the final charges [cf. Eq. (2)]; the higher the value of U_{LCN}, the more rigorous is the constraint on the charge. In Appendix A, we analyze U_{LCN} varying from $U_{\mathrm{LCN}} = 0$ eV to 12 eV, where $U_{\mathrm{LCN}} = 0$ eV corresponds to the case without self-consistency [cf. Eq. (2)]. We compare DOS and Fermi energy, E_f, for different values of U_{LCN}. Our calculations reveal that states in DOS obtained from parametrized TB model without SC ($U_{\mathrm{LCN}} = 0$ eV) are distorted, making the constraint on the local charge neutrality necessary. Our analysis demonstrates that $U_{\mathrm{LCN}} = 8$ eV is an acceptable value [cf. Fig. 8 in Appendix A].

Next, regarding a pertinent value for tol [Eq. (3)], in Appendix A, we start with $tol = 10^{-2}$ and increase the requirement for the convergence to $tol = 10^{-6}$. By taking into account how values of tol influence DOS and E_f, we find that $tol = 10^{-4}$ is an appropriate value [cf. Fig. 9 in Appendix A].

Finally, let us briefly reflect on the degree of self-consistency implemented in this work. Starting from our parametrized TB model that, by definition, artificially assumes no charge transfers, we add a relatively simple function [please see the second term in Eq. (2)] to account for an additional contribution originating from charge fluctuations. In addition to on-site contributions [b=b' in the second term in Eq. (2)], we also have atoms' pairwise interactions depending on the overlap between orbital α of atom b and orbital β of atom b', i.e., $[(Q_b^{\mathrm{Mull}} - Z_b^0) + (Q_{b'}^{\mathrm{Mull}} - Z_{b'}^0)]$, scaled by $S_{\alpha,\beta}^{b,b'}$.

In our approach the total energy is shifted by a constant. In a more rigorous representation of charge fluctuations, one should understand and properly model contributions from Coulomb interaction, and exchange-and correlation, see e.g., Ref. [78]. This however, makes calculations more complex and limits, at least currently, the size of the system that can be analyzed.

Distance scaling of hopping and overlap integrals. In our nanostructured MoS_2 bilayer systems, atoms deviate from their equilibrium positions; this includes edge atoms in individual nanoplatelets after relaxation, and variation of the distance d_c between the top and bottom MLs in our system [cf. Fig. 1(b)]. Given that our employed TB parameter set is derived for atoms at equilibrium positions, as it is a standard procedure, we scale them by engaging the distance scaling constant [81,91–93]. The distance scaling constant includes polynomial and exponential parts, with associating parameters.

In Appendix B, we test a range of parameters, investigating relevance of polynomial and exponential part in the distance scaling constant. We find two sets of parameters in the distance scaling constant, one that describes the displacement of edge atoms in nanoplatelets, and the other that incorporates variation of the distance between MLs, d_c, which interact through vdW type forces. Where applicable, we compared our findings to those extracted from DFT calculations [94,95] and found good agreement [cf. Appendix B].

To encapsulate, within our approach, self-consistency loop is added to our proven parametrized TB model to account for charge transfers between atoms in our nanostructured MoS_2 bilayer systems. We systematically tested parameters of our SCTB model, the local charge neutrality constant and the tolerance, and found optimal values. Next, in order to model variation TB parameters with the deviation of atoms from their equilibrium positions, we modify our TB parameter set by introducing the distance scaling constant. Our systematic analysis led to the two distance scaling constants, one for the nearest-neighbor interaction within the ML or nanoplatelet [cf. Figs. 1(a) and 1(b)], and the other one for vdW-type interaction between the bottom ML and the top ML of the 2D array of nanoplatelets [cf. Fig. 1(b)].

For completeness, we provide a brief overview of how the converged eigenvalues and eigenvectors from our SCTB model are employed to calculate total DOS, density of states projected on atoms and/or orbitals of atoms (pDOS), and the real part of optical conductivity in Appendix C; for additional technical details the reader is referred to Ref. [24].

III. RESULTS AND DISCUSSION

In this study, we focus on understanding the electronic and optical properties of nanostructured bilayers. We explore the interplay between structural features of periodic nanostructures in the top ML of the bilayer, reflected through their size and edge-atom positions, and the distances between them, from one side, and their interaction with the bottom ML of pristine MoS_2 from the other.

For periodic nanostructures in the top ML we adopt triangular nanoplatelets, ranging in the size from the smallest possible triangular nanoplatelets, corresponding to $N_{Mo} = 2$, to nanoplatelets with $N_{Mo} = 4$, which have been experimentally observed [50]. In this way, from a fundamental viewpoint, we are able to understand the competing effects of the edge states versus states from the interior of the triangular nanoplatelets on the optoelectronic properties; for $N_{Mo} = 2$, the edge effects dominate, but reduce with the increase in the size of nanoplatelets. From a practical viewpoint and given recent progress in fabrication [21,46], we reveal distinctive optoelectronic properties of the nanostructured bilayers with nanoplatelets with $N_{Mo} \leqslant 4$, that could stimulate experimental studies of these systems and potentially lead to interesting applications in optoelectronic devices.

We consider the distances between the nanoplatelets in **a** and **b** directions, (d_a, d_b), varying from (d_a, d_b) = (a,a) to (d_a, d_b) = (4a,4a); see Fig. 1(b). We also discuss changes in the electronic structure and optical response if instead of periodic triangular nanoplatelets, we introduce periodic triangular nanoholes.

A. Effect of internanoplatelet distance for cases with $N_{Mo} = 2$

Let us first look at the electronic structure of the individual components of our nanostructured MoS_2 bilayers system, pristine 1ML MoS_2, and triangular MoS_2 nanoplatelets. Whereas, the electronic structure of a single ML of MoS_2 exhibits a finite (direct) band gap, as shown in top panel in Fig. 1(c), the edge atoms in nanoplatelets introduce electronic states in the band gap, changing the character of the material from semiconducting to metallic (see also Refs. [24,27]). As an example, we show the calculated DOS of a Mo_3S_{12} nanoplatelet with $N_{Mo} = 2$ and a Mo_6S_{20} nanoplatelet with $N_{Mo} = 3$ in the bottom panel in Fig. 1(c).

Regarding the electronic properties of nanostructured bilayers, we start with the bilayers containing periodic triangular Mo_3S_{12} nanolatelets with $N_{Mo} = 2$ in the top layer, and consider $(d_a, d_b) =$ (a,a) and $(d_a, d_b) =$ (2a,2a). To visualize the structure we note that, e.g., for $(d_a, d_b) =$ (a,a) the corner S atoms of two neighboring nanolatelets are separated by the lattice constant in both, **a** and **b** directions; see also Fig. 1(b).

Figure 1(d) shows calculated DOS for our nanostructured bilayers We observe the occurrence of the electronic states in what was a band gap in DOS of pristine MoS_2, area in the plot between two vertical dashed lines. The distances between nanoplatelets in the top ML, (d_a, d_b), determine the existence of mini band gaps. For $(d_a, d_b) =$ (a,a), we do not observe any band gaps, but for $(d_a, d_b) =$ (2a,2a) we identify two band gaps of $\sim$0.5 and $\sim$0.6 eV, separated by a peak at ~ -0.15 eV.

Optical responses of our two model nanostructured bilayers, represented via the real part of optical conductivity, $\mathrm{Re}[\sigma]$, are shown in Fig. 1(e); for comparison, we also show $\mathrm{Re}[\sigma]$ of pristine 1ML MoS_2. We draw the reader's attention to the ordinates, where the scale of $\mathrm{Re}[\sigma]$ for 1ML MoS_2 is given on the right ordinate, and differs from the scale for the spectra of the nanostructured bilayers with (a,a) and (2a,2a), which is shown on the left ordinate.

We see that (d_a, d_b) determines the optical properties of these systems. For (a,a), we observe one dominant and broad peak at $\sim$0.67 eV, and for (2a,2a), we see three relatively narrow peaks located at $\sim$0.72, $\sim$0.9, and $\sim$1.5 eV. Interestingly, irrespective of (d_a, d_b), all the peaks are located below the peaks in the spectrum of pristine 1ML MoS_2; they all originate from the transitions between the states of the periodic nanoplatelets in the top ML, and specifically the edge-atom states of nanoplatelets (see the discussion below).

Calculated DOS and spectra of our nanostructured bilayers do not contain any features that could be traced to either pristine ML of MoS_2, or nanoplatelets. Instead, our model systems exhibit the distinctive electronic and optical properties, where by controlling the periodic nanostructure in the top ML of our bilayers, we can tune their electronic properties, such as band gaps, and optical response, i.e., number of peaks and their positions. Also, these distinct features have not been observed in isolated or periodic vertically stacked nanoplatelets, which demonstrated metallic behavior [96].

The origin of the distinctive electronic and optical properties of nanostructured MoS_2 bilayers can be resolved by analyzing the projected DOS on all orbitals of atoms at the top ML of our system. Our results are summarized in Fig. 2.

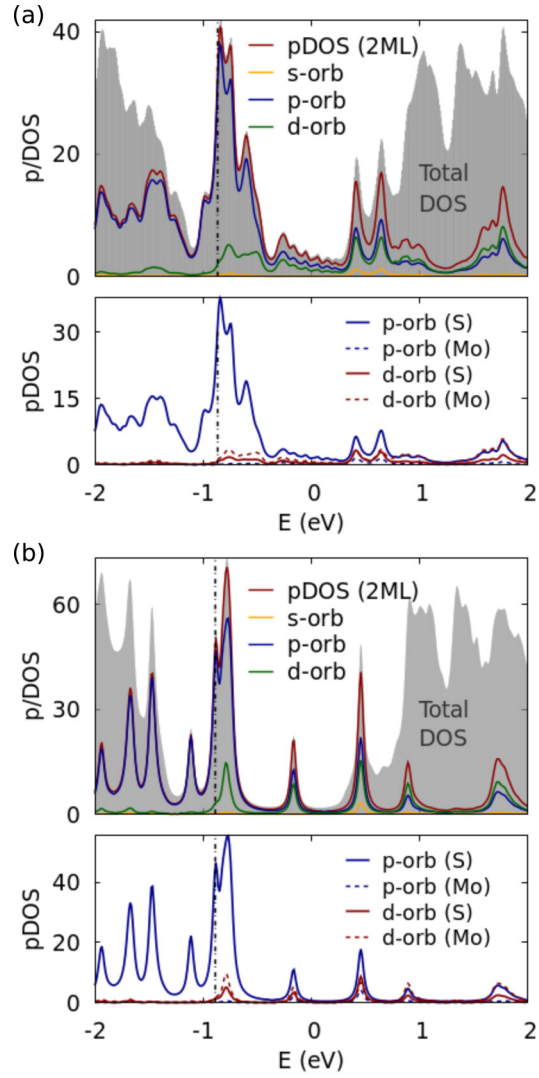

FIG. 2. Calculated total DOS and projected DOS for nanostructured MoS_2 bilayers with (a) $(d_a, d_b) =$ (a,a) and (b) $(d_a, d_b) =$ (2a,2a). Top panels show total DOS (shaded region) and total pDOS of the 2D periodic array of nanomaterials in the top ML, and contributions of s, p, and d orbitals of all S and Mo atoms in the top ML. Bottom panels show calculated contribution of p- and d-orbitals of S and Mo atoms in the top ML. The vertical dash-dotted lines show the position of Fermi energy E_f.

Calculated total DOS and projected DOS on all orbitals of all atoms of nanoplatelets for our nanostructured bilayer with $(d_a, d_b) =$ (a,a) is shown in Fig. 2(a), and for the bilayer with $(d_a, d_b) =$ (2a,2a) in Fig. 2(b). Top panels show the total DOS (shaded region) and projected DOS on orbitals of *all atoms* (Mo and S) of the top ML, i.e., periodic nanoplatelets. The bottom panels show calculated contributions of p and d orbitals of S and Mo atoms of nanoplatelets to the total DOS.

We see that the total DOS for the energies in the interval $[-1.5,0.7]$ eV is predominantly determined by the orbitals of atoms in the top ML, i.e., periodic nanoplatelets. For energies outside that interval, i.e., the energies lower than -1.5 eV or higher than 0.7 eV, the dominant contribution to the total DOS

originates from the orbitals of the atoms in the bottom ML, i.e., pristine 1ML MoS_2.

Resolved by the orbitals of atoms constituting nanoplatelets in the top ML, the primary contribution to total DOS comes from the p orbitals of S atoms for the energies up to ∼0.2 eV, [cf. bottom panels in Figs. 2(a) and 2(b)], and for the energies in the interval [0.2,0.7] eV, in addition to the contribution of p orbitals of S atoms, we also observe the contribution of d orbitals of Mo atoms and d orbitals of S atoms. As it has been commonly found in TMD-based systems [24], contributions of sorbitals of S and Mo atoms are negligible.

Distinct electronic properties of nanoplatelets compared to those of pristine 1ML MoS_2 originate from edges of the nanoplatelets. Edge atom composition, as extracted from experiment [50], reveals the excess S atoms [cf. Figs. 1(a) and 1(b)], which increases the S/Mo ratio compared to the bulk case. Also, all edge atoms have reduced number of neighbors, which implies reduced orbital atom interactions. It was shown that the electronic states arising from Mo and S edge atoms (see also discussion below) have energies close to Fermi level (vertical dashed line in Fig. 2). The edge S atoms introduce p states comparable to the p-d hybridized states near the top of valence band. [23]

Compared to isolated nanoplatelets, our nanostructured bilayer contains a 2D periodic array of nanoplatelets, where nanoplatelets interact between each other as well as with the bottom ML of pristine MoS_2. Whereas the interaction between the nanoplatelets and the bottom ML of MoS_2 is constant, the strength of interaction between the nanoplatelets in the top ML is determined by (d_a, d_b); the number of neighbors of the edge S and Mo atoms, i.e., nonbonding p and d states of the edge S and Mo atoms, varies with (d_a, d_b). Consequently, this is reflected on the electronic properties. If we look at DOS of the two nanostructured bilayers in Fig. 2, DOS of the nanostructured bilayer with $(d_a, d_b) =$ (a,a) does not exhibit either pronounced peaks or band gaps [Fig. 2(a)], but DOS of the nanostructured bilayer with $(d_a, d_b) =$ (2a,2a) have well pronounced peaks and mini gaps, resembling DOS of isolated nanoplatelets [bottom panel in Fig. 1(c)].

Let us elaborate further on the variation of the number of neighbors. Focusing on the nearest neighbors, in the pristine 1ML MoS_2, each S atom has seven nearest-neighbor S atoms (six in plane and one in the other S layer) and three nearest-neighbor Mo atoms. Mo atom has six nearest-neighbor Mo atoms and six nearest-neighbor S atoms (three in each S plane). On the other hand, the number of nearest neighbors of the edge atoms in isolated nanoplatelets, varies depending on the position. Corner edge S atoms have three nearest-neighbor S atoms (two in plane and one in the other S layer), and only one Mo neighbor. Other edge S atoms have five nearest-neighbor S atoms and two Mo atoms. Mo atoms at the edge have six nearest-neighbor S atoms and two Mo atoms.

In the case of the nanostructured bilayer, the number of the nearest neighbors for the edge atoms of the nanoplatelets depends on (d_a, d_b). For $(d_a, d_b) =$ (a,a), corner edge S atoms have five nearest-neighbor S atoms (four in plane and one in the other S layer), and one Mo neighbor, just as in the case of single/isolated nanoplatelets. Other edge S atoms have five nearest-neighbor S atoms and two Mo atoms. Mo atoms at the edge have six nearest-neighbor S atoms and two Mo atoms. For periodic nanplatelets with $(d_a, d_b) \geqslant$ (2a,2a), the number of the nearest neighbors of edge S and Mo atoms is identical to the case of isolated nanoplatelets. Therefore, by controlling (d_a, d_b), we can control the electronic properties of these systems.

We remind the reader that in our nanostructured bilayers, periodic nanoplatelets interact with the bottom ML of pristine MoS_2 through weak vdW forces; in our SCTB model that is included through the second nearest-neighbor S-S hopping and overlap integrals.

Dash-dotted lines in Fig. 2 denote the position of Fermi energy, E_f. E_f is sensitive on the variation of (d_a, d_b); E_f for $(d_a, d_b) =$ (2a,2a) is redshifted compared to E_f for $(d_a, d_b) =$ (a,a) by 26 meV. However, the shift in E_f does not introduce any qualitative differences.

In the light of the previous discussion let us revisit the optical response of our two nanostructured bilayers given in Fig. 1(e). We see that the peaks in the optical spectra up to energies of ∼1.7 eV correspond to the transitions between the occupied states near E_f and empty states in what was the band gap in pristine ML MoS_2, originating from the periodic nanoplatelets in the top ML of our systems. For the nanostructured bilayer with $(d_a, d_b) =$ (a,a), the empty states are spread in the interval [−0.4,0.3] eV [cf. Fig. 2(a)], determining a broad peak in the optical spectrum at ∼ 0.67 eV. For the nanostructured bilayer with $(d_a, d_b) =$ (2a,2a), the empty states exhibit peaks in the interval [−0.4,0.3] eV [cf. Fig. 2(b)], which is reflected in the optical spectrum as three peaks at ∼0.72, ∼0.9, and ∼1.5 eV [Fig. 1(e)].

Interestingly, optical transitions for photon energies $\geqslant$1.7 eV are not *significantly* influenced by the variation of (d_a, d_b) [cf. Fig. 1(e)]. They originate from the electronic states of the bottom, pristine MoS_2 ML, coupled to the ML with periodic nanoplatelets via weak vdW forces, but do not reproduce the two peaks in the spectrum of pristine 1ML MoS_2 [cf. Fig. 1(e)].

Figure 1(e) also reveals optical activity of our nanostructured bilayers for photon energies $\leqslant$0.5 eV. At these energies, the contribution of intraband transitions should also be taken into account. However, these transitions depend on lattice imperfections and temperature and are not considered in this work; the reader is referred to Appendix C and Ref. [24] for additional discussion. Also, our spectra are calculated considering a single-particle picture. Inclusion of excitonic effects would also involve possible transitions for electrons and holes localized in different MLs. For comparison with experimentally measured spectra, one would need to include those effects as well.

Figure 3 shows how total DOS and pDOS on atoms in top ML (left panels), and [Reσ] (right panels) are influenced by the variation of distances between nanoplatelets, (d_a, d_b). For completeness, we also show the cases of (a,a) and (2a,2a), which are already shown in Figs. 1(d) and 1(e).

Calculated total DOS and pDOS for different (d_a, d_b) show that the orbitals of atoms of the top ML have dominant contribution to total DOS up to energies of ∼0.7 eV, where the exact upper limits vary with the variation of (d_a, d_b). In the interval [−0.3,0.3) eV, (d_a, d_b) determines whether a miniband or a single peak in DOS will be created; minibands

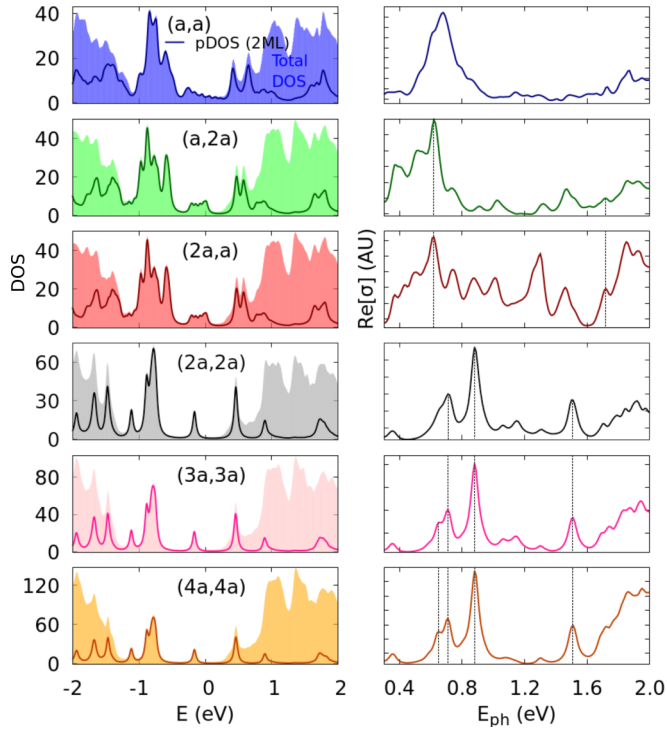

FIG. 3. Calculated total DOS (shaded area) and pDOS (lines) of the states originating from the top ML with periodic nanoplatelets (left) and Re[σ] for different distances between nanoplatelets (d_a, d_b) [see also Fig. 1(b)].

for the bilayers with (a,a), (a,2a), and (2a,a) are replaced by a single peak for the nanostructured bilayers with (2a,2a), (3a,3a), and (4a,4a). In the interval [0.3,0.7) eV, two peaks in DOS of the nanostructured bilayers with (a,a), (a,2a), and (2a,a) are replaced by a single peak for the bilayers with (2a,2a), (3a,3a), and (4a,4a).

These findings are a direct consequence of the variation in the number of (nearest) neighbors for the edge atoms of the nanoplatelets in the top ML of our bilayers. With the increase of (d_a, d_b) from (d_a, d_b) = (a,a) to (d_a, d_b) = (a,2a) [or (d_a, d_b) = (2a,a)], a mini gap of ∼0.25 eV is opening at ∼0 eV. For example, by looking at the nearest-neighbor atoms only, the number of the nearest-neighbor atoms of the two (our of three) corner edge S atoms reduces from five to four. As a side note, we draw the reader's attention to the fact that the total DOS and pDOS of (a,2a) and (2a,a) are identical. This is because of periodicity of our nanostructured bilayers in the **a** and **b** directions [cf. Fig. 1(b)].

With the further increase of (d_a, d_b) to (2a,2a), (3a,3a), and (4a,4a), the miniband transforms to the peak at ∼−0.15eV and we observe the creation of two mini band gaps around the peak (Fig. 3). Also, two peaks in the interval [0.3,0.7) eV of DOS for the bilayers with (a,a), (a,2a), or (2a,a), are replaced by the single peak in DOS of the bilayers with (2a,2a), (3a,3a), and (4a,4a).

The occurrence of peaks in DOS of the bilayers with (2a,2a) (and higher) resembles DOS of isolated nanoplatelets [cf. bottom panel in Fig. 1(c)]. However, compared to DOS of an isolated nanoplatelets, positions of peaks and development of mini band gaps in DOS of the nanostructured bilayers are enabled not only through variation in the size of nanoplatelets, but also through the interaction between the nanoplatelets in the top ML of the bilayer and with the bottom ML of pristine MoS_2.

Next, if we look at [Reσ] (right panels in Fig. 3), the number and width of peaks in the spectra is determined by (d_a, d_b), similar to the variation of the electronic properties with (d_a, d_b). We have already discussed compared the optical response of the bilayers with (d_a, d_b) = (a,a) and (d_a, d_b) = (2a,2a).

Starting from the analyzed spectrum of the nanostructured bilayer with (a,a), which exhibits one dominant and broad peak at ∼0.67 eV, the increase in (d_a, d_b) to (a,2a) or (2a,a) leads to the occurrence of additional peaks in spectra. However, although DOS and pDOS for the bilayers with (2a,a) and (a,2a) are identical, their spectra differ. This is because we consider the polarization in the **a** direction. If we were to consider polarization in **b** direction, we would have a reverse situation with spectra (not shown here). We note that the positions of two peaks in these spectra are aligned, as denoted with the dashed lines in the second and third panels on the right-hand side in Fig. 3.

With the increase of (d_a, d_b) from (2a,2a) to (3a,3a) and (4a,4a), the three dominant peaks located at ∼0.72, ∼0.9, and ∼1.5 eV in the spectrum of the bilayer with (2a,2a) persist at approximately same energies. The reason for the existence (and alignment) of these peaks can be traced back to the peaks and mini band gaps in DOS of these nanostructured bilayers, originating from the edge atoms of the nanoplatelets in the top ML of the bilayers (discussed above). Interestingly, an additional peak red shifted in energy compared to ∼0.72 eV peak, appears in the spectra of the bilayers with (3a,3a) and (4a,4a) (bottom two plots on the right-hand side in Fig. 3). We also note the existence of peak at ∼0.35 eV for the bilayers with (2a,2a), (3a,3a), and (4a,4a). However, we do not discuss the transitions at low energies, as intraband transitions, which are not included in our model, could have significant influence; see also our previous discussion and Appendix C.

In the spectra of all considered nanostructured bilayers, for photon energies $\geqslant$1.7 eV, optical response originate from the transitions between the states in the bottom ML, i.e., pristine MoS_2 ML, interacting through weak vdW forces with the top ML with periodic nanoplatelets; the influence of top ML is only reflected through the intensity of the transitions in this region.

B. Effect of positions of edge sulfur atoms

In the interplay between the edge atoms of the nanoplatelets and the distances between nanoplatelets in the top ML, the electronic and optical properties of our nanostructured bilayers are determined. Whereas we could expect to tune (d_a, d_b) in the experiment with reasonable accuracy, the full control of the edge-atom positions could be challenging. In order to investigate how even modest variations of positions of the edge atoms of nanoplatelets in the top ML influence the electronic and optical properties of our nanostructured bilayers, we artificially modify the edge-atom positions in nanoplatelets.

We consider a nanostrucuted bilayer with $(d_a, d_b) = (2a,2a)$, and nanoplatelets where edge-atom are in (i) relaxed atomic positions, (ii) ideal (bulklike) positions, (iii) artificially modified starting from relaxed positions, so the distance between edge S atoms in **c** direction is reduced, denoted as $dr^{(1)}_{edges}$, (iv) artificially modified starting from relaxed positions, but the distance between edge S atoms in **c** direction is increased, $dr^{(2)}_{edges}$, and (v) relaxed edge-atom positions, but with the distance between MLs, the bottom pristine MoS_2 ML, and top ML with periodic nanoplatelets, is increased by 5%, $d_c^{ideal} \rightarrow c_{var}$. Our results are summarized in Fig. 4.

Figure 4(a) shows the calculated DOS for our model nanostructured bilayer and different edge-atom positions. We see that only DOS of the nanostructured bilayer with the ideal (bulklike) edge-atom positions qualitatively differs from DOS of the bilayers with other considered edge-atom configurations. Specifically, in the energy interval $[-0.3,0.3]$ eV, DOS of the bilayer with ideal edge-atom positions exhibits two peaks, wheres DOS of all other considered bilayers shows only one peak.

However, if we look at the optical response, $[Re\sigma]$, shown in Fig. 4(b), we see that, whereas the positions of peaks are influenced by the edge-atom positions, there are always three dominant peaks in the spectra. Also, for the transition energies $\geqslant$1.7 eV, we see that spectra for the bilayers with different edge-atom positions are very similar, which is expected given that this part of the spectra originates from the transitions between states in the bottom ML of pristine MoS_2. However, the spectrum of the nanostructured bilayer with ideal, bulklike positions of edge atoms do not reveal low intensity peaks, e.g., for the photon energies in the interval [1.0,1.4] eV.

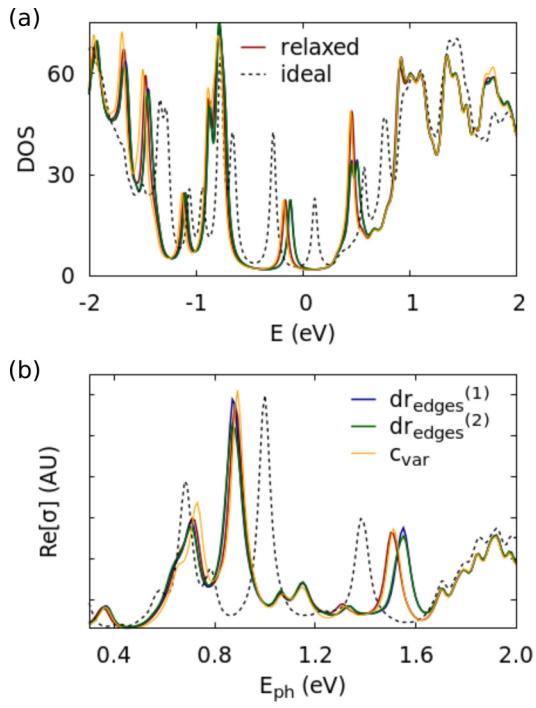

FIG. 4. Calculated DOS (a) and $[Re\sigma]$ (b) for (2a,2a) periodic MoS_2 nanomaterial system, with different position of edge atoms, ranging from ideal bulk atom positions, relaxed atom positions, artificially modified positions, $dr^{(1)}_{edges}$ and $dr^{(2)}_{edges}$ (see text), and with increased distances between the layers by 5%, $d_c^{ideal} \rightarrow c_{var}$.

Overall, the variations of edge-atom positions are directly reflected in the electronic properties and optical response of nanostructured bilayers. The analysis of the nanostructured bilayers with ideal, bulklike positions of edge atoms is not sufficient to provide the correct description of the electronic properties, but it does reproduce three dominant peaks in the spectra, agreeing qualitatively with spectra of the nanostructured bilayers with realistic and artificially modified edge-atom positions.

C. Influence of S/Mo ratio in nanoplatelets

Within our SCTB approach, we have revealed the electronic and optical properties of the nanostructured MoS_2 bilayers with the nanoplatelets with edge configuration with 100% S coverage, shown in Fig. 1(a). Lauritsen *et al.* suggested that smaller nanoplatelets could have reduced S concentration at the edges [50], where S coverage got reduced from 100% [see, e.g., Fig. 1(a)] to 75% and 50% (see top panels in Fig. 5(a) and also Ref. [50]). We discuss how those changes at the edges influence the electronic and optical properties. Our results are summarized in Fig. 5 for nanostructured bilayers with $(d_a, d_b) = (2a,2a)$.

Top panels in Fig. 5(a) show edges of two nanoplatelets with reduced S coverage at the edge, Mo_3S_6 nanoplatelets with edges with 50% S coverage (left panel), and Mo_3S_9 nanoplatelets with edges with 75% S coverage (right panel). Top ML of our model nanostructured bilayer consists of 2D array of these nanoplatelets.

We show the calculated total DOS (shaded region) and pDOS of the 2D periodic array of nanoplatelets in the top ML, and contributions of *s*, *p*, and *d* orbitals of all S and Mo atoms in the top ML. Bottom panels show calculated contribution of *p* and *d* orbitals of S and Mo atoms in the top ML. The vertical dash-dotted lines show the position of E_f.

We see that irrespective of edge configurations of nanoplatelets the electronic states, originating from the atoms of the ML with periodic nanoplatelets get embedded between electronic states of pristine MoS_2 ML. For 50% S-coverage [left panels in Fig. 5(a)] and 75% S coverage [right panels in Fig. 5(a)], the total DOS for the energies in the interval $[-1.6,0.4]$ eV and $[-1.3,0.7]$ eV, respectively, is predominantly determined by the orbitals of atoms in the top ML, i.e., periodic nanoplatelets. For energies outside those intervals, the dominant contribution to the total DOS originates from the orbitals of the atoms in the bottom ML, i.e., pristine 1ML MoS_2. This is in agreement with systems with 100% S coverage (cf. Fig 2).

In all of the considered cases, the electronic states of the periodic nanoplatelets originate primarily from *p* orbitals of S atoms and *d* orbitals of Mo atoms. As expected, reducing of S coverage at the edge increases the contribution of *d* orbitals of Mo atoms, e.g., compare bottom panel in Fig. 2(b) and bottom panels in Fig. 5(a).

Figure 5(b) shows how the calculated DOS for our model nanostructured bilayers with the periodic nanoplatelets with 50% and 75% S coverage compare to DOS of the nanostructured bilayers with nanoplatelets with 100% S coverage.

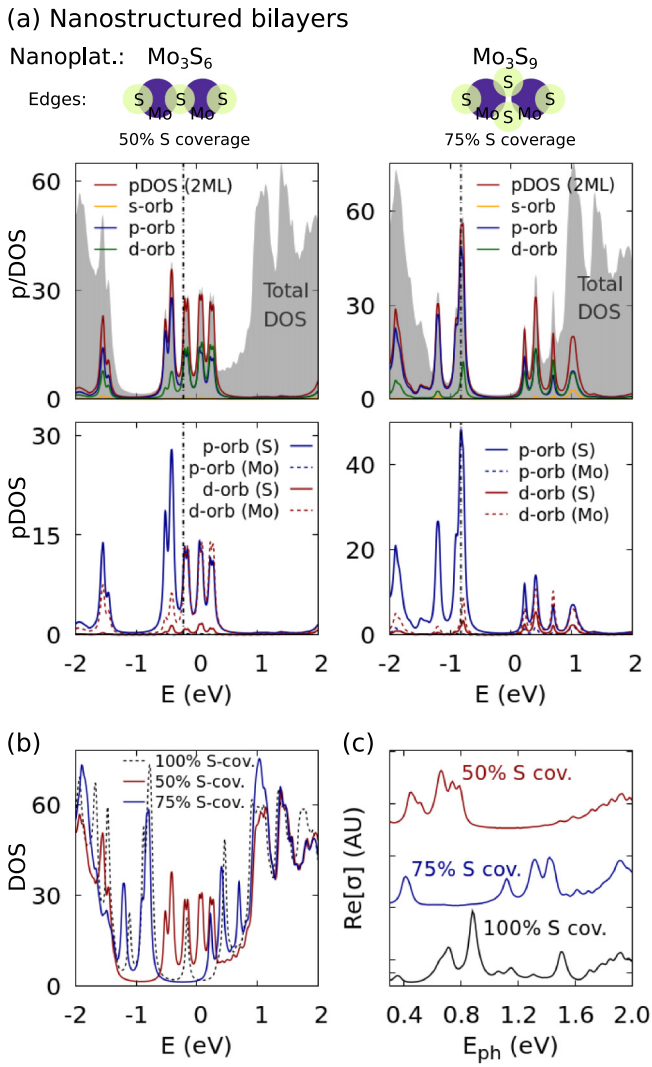

FIG. 5. (a) For nanostructured bilayers with $(d_a, d_b) = (2a,2a)$ and triangular nanoplatelets with edge configurations with 50% and 75% S coverage (edges are shown schematically in top left and right panels, respectively), calculated total DOS (shaded region) and pDOS of the 2D periodic array of nanoplatelets in the top ML, and contributions of s, p, and d orbitals of all S and Mo atoms in the top ML. Bottom panels show calculated contribution of p and d orbitals of S and Mo atoms in the top ML. The vertical dash-dotted lines show the position of E_f; calculated total DOS (b) and optical response (c) of nanostructured bilayers with nanoplatelets with edge configurations with 50%, 75%, and 100% S coverage.

We see that mini band gaps occur in DOS of all considered systems. However, S coverage determines the position and size of the band gap. Specifically, for the nanostructured bilayer consisting of periodic nanplatelets with 50% S coverage, our calculations reveal the band gap of ∼0.9 eV redshifted compared to E_f, for bilayers with the nanplatelets with 75% S coverage, the band gap of ∼1.0 eV is exposed in DOS, but is blueshifted with respect to E_f. We remind the reader that for nanostructured bilayers with nanoplatelets with 100% S coverage, two mini band gaps of ∼0.5 and ∼0.6 eV were created, separated by a peak in DOS, and blueshifted compared to E_f [cf. Fig. 2(b)].

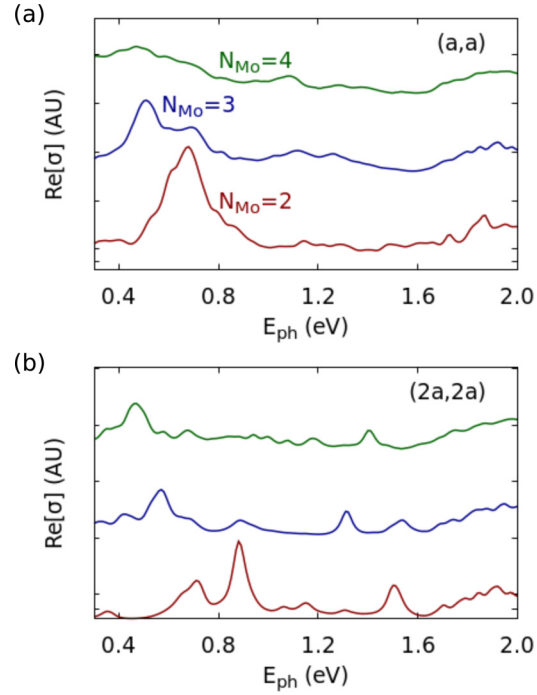

FIG. 6. Calculated real part of optical conductivity, [Reσ], for different sizes of nananoplatelets in the 2D array, $N_{Mo} = 2$, 3, and 4, and distances between nanplatelets, (a) (d_a, d_b) = (a,a), and (b) $(d_a, d_b) = (2a,2a)$.

Next, the influence of the edge configurations of nanoplatelets of our model nanostructured bilayers on [Reσ] is shown in Fig. 5(c). We see that spectra of all considered nanostructured bilayers exhibit optical activity. Specifically, as already discussed [cf. Figs. 1(e) and 6], the spectrum of the nanostructured bilayers with periodic nanoplatelets with 100% S coverage exhibits three dominant peaks at ∼0.72, ∼0.90, and ∼1.50 eV, and one lower intensity peak at ∼0.35 eV. We see that reduced S coverage from 100% to 75% does not change the number of peaks, but determines their positions: low intensity peak at ∼0.35 eV gets blueshifted to ∼0.40 eV, and three dominant peaks at ∼0.72, ∼0.90, and ∼1.50 eV now occur at the transition energies ∼1.10, ∼1.30, and ∼1.45 eV. With reducing S coverage further, which corresponds to the nanostructured bilayer with periodic nanoplatelets with %50 S coverage, the spectrum reveals a peak at ∼0.50 eV, which is broader than low-transition energy peaks in the spectra of our model systems with nanoplatelets with 75% and 100% S coverage at the edge, and three peaks localized in the transition energy interval (0.65,0.80) eV. Given that spectra for the transition energies $\geqslant$1.7 eV originate from the transitions between states in the bottom ML of pristine MoS_2, variations of the S concentration at the edges of the periodic nanoplatelets in the top ML are not reflected in that range of transition energies.

Overall, irrespective of the edge-atom composition, the electronic states which originate from the atoms of the top ML with periodic nanoplatelets get embedded between the electronic states of pristine MoS_2 ML. However, positions and intensity of the peaks in the spectra by the edge-atom

configurations. This includes not only reduced S coverage [Fig. 5(c)], but also variations in edge-atom positions [Fig. 4(b)].

D. Size effect of nanoplatelets

Next, we address how the increase in size of nanoplatelets influences the optical response of our nanostructured bilayers. We consider Mo_6S_{20} nanoplatelets with $N_{Mo} = 3$ and $Mo_{10}S_{30}$ nanoplatelets with $N_{Mo} = 4$. Our results are shown in Fig. 6(a) for (d_a, d_b) = (a,a) and Fig. 6(b) for (d_a, d_b) = (2a,2a). For comparison, we also show the calculated [Reσ] for the bilayer with nanoplatelets $N_{Mo} = 2$.

For the nanostructured bilayer with (d_a, d_b) = (a,a), one dominant and broad peak at $E_{ph} \sim$ 0.67 eV for $N_{Mo} = 2$ gets redshifted and broadened with the increase in the nanoplatelets' sizes, to $N_{Mo} = 3$ and 4. For higher photon energies of up to 1.6 eV, the optical activity is rather low, irrespective of the size of the nanoplatelets. For photon energies $\geqslant$1.7 eV, we observe the increased optical activity, which originates from the bottom, pristine MoS_2 ML, and is not noticeably affected by the top ML.

For nanostructured bilayer with (d_a, d_b) = (2a,2a), the increase in the size of the nanoplatelets, leads to the suppressing of the intensity of peaks, i.e., the three dominant peaks in the spectrum of the bilayer with $N_{Mo} = 2$ nanoplatelets get suppressed in the spectrum of the bilayer with $N_{Mo} = 3$ nanoplatelets, and almost entirely suppressed in the spectrum of the bilayers with the nanoplatelets with $N_{Mo} = 4$. For the nanostructured bilayer with the nanoplatelets with $N_{Mo} = 4$, there is only one dominant, and broad peak redshifted in energy compared to the low energy peaks in the spectra of $N_{Mo} = 2$ and 3 systems.

Optical activity increases for photon energies $\geqslant$1.7 eV, which, as already discussed, originates from the transitions between the states in the bottom, pristine MoS_2 ML. This feature seems to be a common fingerprint of our nanostructured bilayer systems and is not affected by the size of nanoplatelets, (d_a, d_b), or the edge-atom positions.

The variation of the optical response with the size of the nanoplatelets in our systems can be traced back directly to the role of the edge-atom states; larger the size of nanoplatelets, smaller is the influence of the edge states. Therefore the decrease in the optical response, i.e., in number and intensity of peaks, is directly related to the increase in the nanoplatelet's size. This conclusion is valid also for nanostructured bilayers with periodic nanoplatelets with 50% and 75% S coverage.

E. Effect of holes

Finally, we consider nanostructured bilayers, where nanoplatelets in the top ML are replaced by holes, surrounded by MoS_2, i.e., it is an "inverse structure" to our initial structure, where we now have periodic triangular holes in MoS_2 matrix in the top ML. We consider nanostructured bilayers with holes separated by (d_a, d_b) = (a,a) and (d_a, d_b) = (2a,2a).

Figure 7(a) shows calculated total DOS and pDOS on all orbitals and atoms in the top ML of the nanostructured bilayers with holes; left panels refer to our findings for the bilayer with periodic holes separated by (d_a, d_b) = (a,a) and right panels for the bilayer with (d_a, d_b) = (2a,2a).

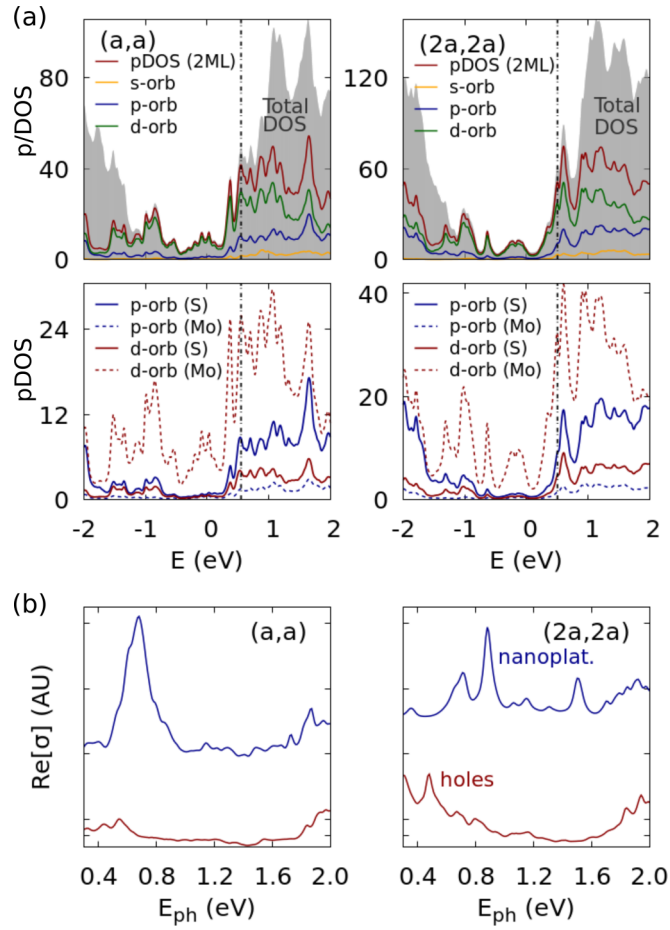

FIG. 7. (a) Calculated total DOS and partial DOS for periodic, triangluar holes instead of nanoplatelets in the top layer with (a) (d_a, d_b) = (a,a) in left panels and (d_a, d_b) = (2a,2a) in the right panels. Top panels show total DOS (shaded region) and total pDOS of the 2D periodic array of holes in the top ML, and contributions of s, p, and d orbitals of all S and Mo atoms in the top ML. Bottom panels show calculated contribution of p and d orbitals of S and Mo atoms in the top ML. The vertical dash-dotted lines show the position of Fermi energy, E_f; (b) calculated real part of optical conductivity, [Reσ], for the case of nanoplatelets replaced by holes in the second layer with different distances (d_a, d_b) = (a,a) (left) and (d_a, d_b) = (2a,2a) (right). For comparison, we also show how the spectra for periodic nanoplatelets with (a,a) and (2a,2a).

We see that the total DOS for energies in the interval $[-1.2,0.9]$ eV is predominantly determined by the orbitals of the atoms in the top ML. Resolved by the orbitals, unlike the case of periodic nanoplatelets where the leading contribution to total DOS originated from p orbitals of edge S atoms, irrespective of (d_a, d_b), for the bilayers with the periodic holes, the leading contribution originates from d orbitals of Mo atoms [bottom panels in Fig. 7(a)]. We also note relevant contribution of p orbitals of S atoms. As already mentioned, contribution of s orbitals of S and Mo atoms to total DOS in TMD-based systems is negligible [24].

Unlike nanoplatelets, where Mo edge atoms are fully covered with S atoms [cf. Fig. 1(a)] and consequently the dominant contribution to total DOS comes from p orbitals of S atoms, nanoholes contain Mo edge atoms not covered with S

atoms. This leads to the reduced number of neighbors of Mo edge atoms and consequently nonbonding d orbitals, which determine the electronic states in what was the band gap in 1ML of pristine MoS_2.

Dash-dotted lines in Fig. 7(a) denote the position of E_f. E_f of nanostructured bilayers with periodic holes is blueshifted compared to our nanostructured bilayers with periodic nanoplatelets, by ∼1.3 eV. Also, E_f for $(d_a, d_b) =$ (2a,2a) is redshifted compared to E_f for $(d_a, d_b) =$ (a,a) by 42 meV.

Figure 7(b) shows calculated [Reσ] for our nanostructured bilayers with periodic holes in the top ML. For comparison we show [Reσ] for the bilayers with the periodic nanoplatelets with (a,a) and (2a,2a) in the top ML. Optical activity for the nanostructured bilayers with periodic holes is observed for the transition energies up to 0.6 eV, and transition energies $\geqslant$1.7 eV.

In the lower energy range (up to 0.6 eV), calculated [Reσ] originates from the transitions from the occupied states of what was the band gap in pristine 1ML MoS_2 and empty states around E_f. However, for this range of transition energies we should also consider the contribution of intraband transitions that is not included in our model. These transitions depend on lattice imperfections (and temperature), and are very often model via phenomenological expression (see Appendix C and Ref. [24]).

At the other end of the calculated spectrum, optical transitions for photon energies $\geqslant$1.7 eV originate from the electronic states of the bottom, pristine MoS_2 ML, coupled to the top ML with the periodic nanoholes via weak vdW forces. This part of spectrum is very similar to the spectra nanostructured bilayers with periodic nanoplatelets irrespective of (d_a, d_b).

Interestingly, whereas the spectra for the bilayers with periodic nanoplatelets in the interval [0.5,1.6] eV is very sensitive to (d_a, d_b) [cf. see Fig. 7(b)], the spectra of the bilayers with periodic nanoholes display very little optical activity irrespective of (d_a, d_b). The reason for weak optical response lies in the reduced orbital interaction of edge Mo atoms and the d-orbital character of empty states around E_f ($d_{x^2-y^2}$) and occupied states in the energy interval (−1.0, −0.5) eV, d_{z^2}. Next, the insensitivity of the spectra on (d_a, d_b) for the bilayers with nanoholes originates from the fact that edge atoms of the MoS_2 matrix surrounding nanoholes are not affected by the variation of the distances between holes. Whereas the variation in the distances between nanoholes quantitatively influence the electronic structure [compare left and right panels in Fig. 7(a)], it does not affect optical properties, which are mainly determined by the edge atoms. Given this analysis, nanostructured bilayers with periodic nanoplatelets are more useful for the optoelectronic properties, specifically with the ability to control number and positions of peaks in the optical spectra, but also to control localization of carriers in the top ML.

F. Discussion

Overall, our findings suggest that it is possible to tune the electronic and optical properties of MoS_2-based nanostructured materials in controllable fashion, opening pathways for potential applications in different optoelectronic devices. Specifically, we have shown that the choice of the periodic nanostructures in the top ML of the nanostructured bilayers, whether they are nanoplatelets or holes, Fig. 1 versus Fig. 7, edge atoms and their positions (Figs. 4 and 5), the distances between nanoplatelets (Fig. 3), and the interaction with the bottom ML of pristine MoS_2 determine the electronic and optical properties of these systems.

Recent experimental reports demonstrated the fabrication of TMD-based nanostructures with an impressive control at subnanometer scales [21,25,46,50,55,97,98]. Structural characterization revealed structures ranging from nanoplatelets

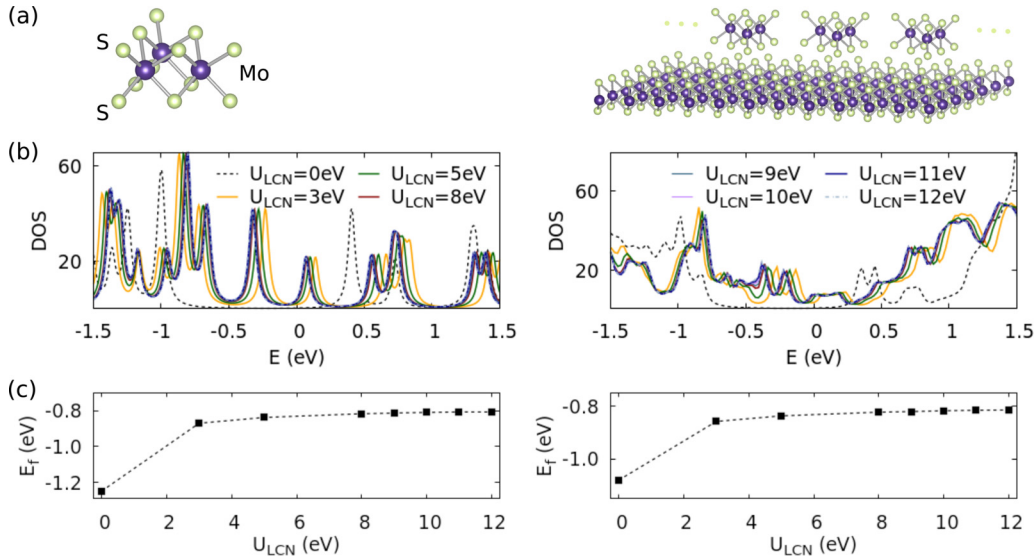

FIG. 8. (a) Structure of Mo_3S_{12} nanoplatelet (left) and nanostructured MoS_2 bilayer with periodic Mo_3S_{12} nanoplatelets in a direction (right) and (b) calculated DOS for different values of U_{LCN} for nanoplatelet (left) and nanostructured bilayer (right). ULCN = 0 eV removes self-consistency loop, reducing our SCTB to a parametrized TB model, and (c) variation of the calculated Fermi energy, E_f with U_{LCN} for the nanoplatelet (left), and nanostructured bilayer (right).

and nanowires [16,21,46,50], vertical and lateral heterostructures [25,26], including WS_2 nanoplatelets within MoS_2 2D matrix and their vertical stacking [16,46], to ML alloys of MoS_2-WS_2 and $MoSe_2$-WSe_2 [46].

Thus we could expect to tune (d_a, d_b) in the experiment with reasonable accuracy, but the full control of an exact edge atoms decoration and the edge-atom positions is not easily achievable. We have demonstrated (cf. Fig. 4) how the variation of the edge-atom positions, including relaxed atomic positions, ideal positions, or artificially modified positions of the edge atoms, do not qualitatively influence the electronic properties, but it does determine the number, positions, and intensities of peaks in the optical spectra. Similarly, variation of S concentration at the edges of nanoplatelets in our model nanostructured bilayers (we considered reduction from 100% to 75% and down to 50%) does not qualitatively influence electronic and optical properties, but can be used to control creation and position of band gaps [Fig. 5(b)] as well as positions of peaks in the optical response [Fig. 5(c)]. At this point, a detailed theoretical model, such as, e.g., the SCTB implemented here, from one side and proper experimental setup enabling fabrication and structural characterization with high, atomic scale precision, including potential revealing of vacancies in interior of nanoplatelets from the other, could open new interesting research questions and potentially lead to new nanostructured bilayers with optimized optoelectronic properties, perhaps also tunned for targeted applications.

Furthermore, given that ML-TMDs are chemically inert and the dispersive nature of vdW forces, they can be coupled with different materials through weak vdW forces. For example, one can embed ML-TMDs in various heterostructures (e.g., silicon-based ones) with a net result of increased performance and functionality, or combine TMDs with graphene or other layered materials to create hybrid nanostructures [3]. Thus it is reasonable to expect that our model systems can be fabricated; consequently, predictions of this work could potentially inspire further experimental studies of these systems.

IV. SUMMARY

We reported a theoretical study of the electronic and optical properties of nanostructured MoS_2 bilayers, which consist of vertically stacked ML of MoS_2 and periodic triangluar nanoplatelets and holes. We demonstrated that the interplay between edge atoms in periodic nanoplatelets or holes, their sizes, and distances between them, controlled the appearance and size of the band gaps, and optical response.

Our calculations of the electronic structure revealed the electronic states, originating from the atoms of the ML with either periodic nanoplatelets or holes, got embedded between electronic states of pristine MoS_2 ML, but with red- and blueshifted valence and conduction bands, respectively. For a ML with periodic nanoplatelets, electronic states originate primarily from p orbitals of S atoms, and for a ML with periodic holes, they originate from d orbitals of Mo atoms.

Whereas the nanostructured bilayers with periodic holes exhibited rather poor optical response, the bilayers with periodic nanoplatelets, irrespective of nanoplatelets' edge configurations exhibited rich optical properties, characterized by the number and intensity of peaks. The calculated real part of optical conductivity showed that the lowest optical transitions originated from the optical transitions within the top ML, containing periodic nanoplatelets. The size of the nanoplatelets and the distance between them, determines the number and the intensity of the peaks in the spectra.

Overall, our findings suggest that it is possible to tune the electronic and optical properties of MoS_2-based nanostructured materials in controllable fashion. Given that fabrication of different TMD-based systems have been already demonstrated, we expect our study to inspire further theoretical and experimental work on this subject, and potentially open pathways for potential applications in different optoelectronic devices.

ACKNOWLEDGMENT

We thank F. Zahid for the discussion regarding the TB parameter set for MoS_2 [74,75].

APPENDIX A

In Sec. II B, we discuss technical details of introducing the self-consistency loop to our parametrized TB model, please see Eqs. (1)–(3). Predictions of our SCTB model depend on the value of the local charge neutrality constant, U_{LCN} [cf. Eq. (2)]. Also, we need to establish how strict limits we should impose on the convergence, i.e., what would be the appropriate value for tol [cf. Eq. (3)].

Here, we test a range of values for parameters U_{LCN} and tol, using two test MoS_2-based systems shown in Fig. 8(a). The first system is a Mo_3S_{12} and $N_{Mo} = 2$ nanoplatelet, left panel in Fig. 8(a), and the second is a nanostructured MoS_2 bilayer system, with 1ML MoS_2 in the bottom layer and an array of Mo_3S_{12} nanoplatelets in the second layer, right panel in Fig. 8(a).

Local charge neutrality constant, U_{LCN}. We analyze U_{LCN} varying from $U_{\mathrm{LCN}} = 0$ to 12 eV, where $U_{\mathrm{LCN}} = 0$ eV corresponds to the case without self-consistency [cf. Eq. (2)].

We compare DOS and Fermi energy, E_f, calculated for different values of U_{LCN}. Our results are summarized in Fig. 8(b) for DOS, and in Fig. 8(c) for E_f; left panels show DOS and E_f for our model nanoplatelet and right panels to DOS and E_f for our nanostructured bilayer system.

For $U_{\mathrm{LCN}} = 0$ eV, we see that, irrespective of the analyzed test system, a nanoplatelet or a nanostructured MoS_2 bilayer, DOS for U_{LCN} reveals artificial band gaps, and E_f differs significantly from E_f extracted from SCTB with nonzero U_{LCN}. This suggests that the parametrized TB method is not sufficient for this type of analysis and that self-consistent calculations are required.

With the increase of U_{LCN}, calculated DOS changes, and artificial band gaps get smaller. For $U_{\mathrm{LCN}} \geqslant 8$ eV, calculated DOS are basically indistinguishable in the energy interval $[-1.5,1.5]$ eV.

Next, regarding E_f, in the absence of self-consistency in our calculations, i.e., $\mathrm{U_{LCN}} = 0$ eV, E_f is significantly lower compared to E_f for any of the nonzero $\mathrm{U_{LCN}}$ cases. For example, $E_f(U_{\mathrm{LCN}} = 0\ \mathrm{eV}) - E_f(U_{\mathrm{LCN}} = 3\ \mathrm{eV}) = -379$ meV for the model nanoplatelet [left panel in Fig. 8(a)] and $E_f(U_{\mathrm{LCN}} = 0\ \mathrm{eV}) - E_f(U_{\mathrm{LCN}} = 3\ \mathrm{eV}) = -222$ meV for the model nanostructured MoS_2 bilayer [right panel in Fig. 8(a)].

With the increase of U_{LCN}, E_f increases, but at much smaller rate; for example, the difference $E_f(U_{LCN} = 8\ \text{eV}) - E_f(U_{LCN} = 12\ \text{eV}) \leqslant 10$ meV for either of our two model systems.

Numerically, we focused on the [3,12] eV interval for U_{LCN}. We note that higher the value of U_{LCN}, the more rigorous is the constraint on the final charges; for example, in an asymptotic case of $U_{LCN} \to \infty$, $Q_b^{\text{Mull}} = Q_b^0$. Therefore, given our presented findings, especially calculated DOS for different values of U_{LCN}, and the corresponding discussion, we adopt $U_{LCN} = 8$ eV in our calculations in the main body of the manuscript.

Tolerance in our SCTB calculations. Convergence criterion in our SCTB calculations is defined by Eq. (3). Value of tol determines the accuracy of our calculations, and the number of iterations N_{iter} required to achieve that accuracy. We use our two test systems shown in Fig. 8(a), and calculate DOS and E_f for different values of tol. We start from $tol = 10^{-2}$ and increasing the requirement for the convergence to $tol = 10^{-6}$.

Calculated DOS and E_f for our model nanoplatelet [cf. left panel in Fig. 8(a)], as they vary for different tol, are shown in Figs. 9(a) and 9(b), respectively. For our nanostructured MoS_2 bilayer system [cf. right panel in Fig. 8(a)], Figs. 9(c) and 9(d) show calculated DOS and E_f, respectively.

Calculated DOS for $tol = 10^{-2}$ differs significantly from those calculated adopting $tol = 10^{-3}$ and higher. However, starting from $tol = 10^{-3}$, we see that irrespective of our model system, a nanoplatelet or a nanostructured bilayer, calculated DOS is indistinguishable from DOS obtained with increased accuracy, 10^{-4} and higher; see top panels in Figs. 9(a) and 9(b) for the calculated DOS of a nanoplatelet and nanostructured bilayer, respectively.

Next, E_f obtained adopting $tol = 10^{-2}$, is noticeably overestimated compared to E_f calculated assuming higher accuracy, $tol = 10^{-3}$ and higher; for example, for our model nanoplatelet [left panel in Fig. 8(a)], $E_f(tol = 10^{-2}) - E_f(tol = 10^{-3}) = 18$ meV, and for our model nanostructured MoS_2 bilayer [right panel in Fig. 8(a)], $E_f(tol = 10^{-2}) - E_f(tol = 10^{-3}) = 64$ meV. With the further increase in the accuracy, variation in E_f for $tol = 10^{-3}$ to $tol = 10^{-6}$, are less than 0.2 meV for the nanoplatelet, and less than 5 meV for the nanostructured bilayer.

In our calculations in the main body of the manuscript, we chose $tol = 10^{-4}$ because $E_f(tol = 10^{-4}) - E_f(tol = 10^{-6}) = 0.4$ meV for the nanoplatelet, and $E_f(tol = 10^{-4}) - E_f(tol = 10^{-6}) = 0.2$ meV for the nanostructured bilayer. We note that results reported in Appendix A (Figs. 8 and 9) are obtained for $tol = 10^{-4}$.

In addition, it is interesting to note that if we look at the number of iterations N_{iter}, needed to achieve desired accuracy, we see that the convergence for the case of the nanoplatelet [left panel in Fig. 8(a)] requires significantly larger N_{iter}. For example, for $tol = 10^{-4}$, requires $N_{\text{iter}} = 100$ for the nanoplatelet and $N_{\text{iter}} = 9$ for the nanostructured bilayer. Given that there are no qualitatively differences in the electronic structure of the nanoplatelet and nanostructured bilayer with the increase tol from $tol = 10^{-3}$ to $tol = 10^{-4}$, SCTB calculations with $tol = 10^{-3}$ could also be a reasonable compromise between accuracy and the number of iterations [see e.g., Fig. 9(b)].

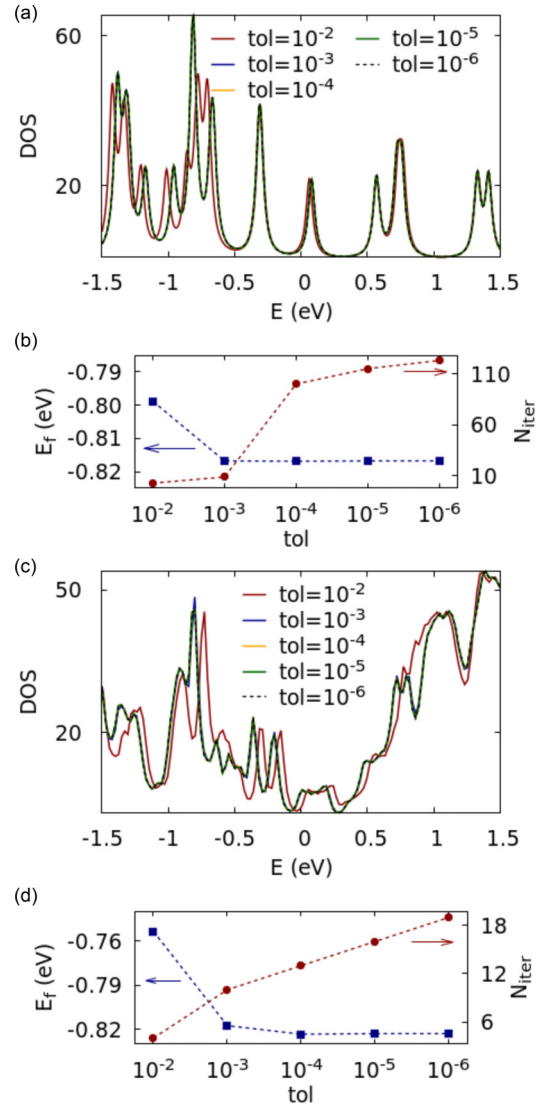

FIG. 9. (a) Calculated DOS for different values of the convergence constraint tol for nanoplatelet given in left panel in Fig. 8(a); (b) calculated Fermi energy E_f for the nanoplatelet for different values of tol and number of iterations N_{iter} needed to achieve the convergence; (c) the same as (a) but for nanostructured bilayer system given in right panel in Fig. 8(a); and (d) the same as (c) but for the nanostructured bilayer.

APPENDIX B

It is well known that within a TB approximation, deviation of atoms from the equilibrium atomic position requires introducing the distance scaling of hopping and overlap integrals [81,92]. Within our TB implementation for TMD-based materials, we employ the TB parameter set for MoS_2 as introduced by Zahid *et al.* in Refs. [73–75]. This parameter set has been successfully employed in our TB model to extract the electronic structure of pristine and nanostructured MoS_2 [24,27,41]. Here we investigate relevant parameters for the distance scaling constant, required for modeling of the nearest-neighbor interactions between atoms away from their equilibrium positions and also S-S second nearest-neighbor interactions simulating vdW forces between MoS_2 ML and the nanostructure [cf. Fig. 1(b)].

The distance scaling of hopping and overlap integrals is treated as follows [81,92]:

$$V_{ijk}(r) = V_{ijk}(r_0) \cdot f(r_0, r)\,, \tag{B1}$$

where $V_{ijk}(r_0)$ and $V_{ijk}(r)$ denote hopping (or overlap) integrals for atoms in equilibrium positions and perturbed from the equilibrium positions, respectively; $f(r_0, r)$ is the distance scaling constant, which is given by [81,92]

$$f(r_0, r) = \left(\frac{r_0}{r}\right)^{\tau} \exp\left\{-n_{\text{exp}}\left[\left(\frac{r}{r_c}\right)^{n_c} - \left(\frac{r_0}{r_c}\right)^{n_c}\right]\right\}, \tag{B2}$$

where τ, n_{exp}, r_c, and n_c are parameters.

Typically, the Harrison universal form is adopted [81,93]. This includes the following values for the parameters in Eq. (B2): $n_{\text{exp}} = 0.0$, and τ depends on the orbitals in the hopping integral; for s-s, s-p, and p-p, $\tau = 2.0$, for s-d and p-d, $\tau = 3.5$, and for d-d, $\tau = 5.0$.

However, it was typically assumed that this $(r_0/r)^{\tau}$ dependence is valid near the equilibrium atomic positions, but could break down at larger separations [91,92]. Given that we also model vdW type interactions, and the fact that the atomic functions decay exponentially, within our TB implementation we test parameters for distance scaling that include exponential term as well [cf. Eq. (B2)].

In this Appendix, we test a range of parameters in the distance scaling constant to account for the variations of (i) the interlayer separation, i.e., variation of the vdW type forces, which are in our model included through second nearest-neighbor S-S interactions [24] and (ii) the distances between nearest neighbors in the nanostructure [cf. Figs. 1(a) and 1(b)]. In what follows, we analyze (i) and (ii) in a greater detail and, where possible, compare our findings with results already reported in literature.

First, to find parameters in the distance scaling constant for the variation of the inter-layer separation [see d_c in the right panel in Fig. 1(a)], we consider 2ML MoS_2, as shown in Fig. 10(a). This system is chosen because there are recent DFT calculations available for us to make comparison.

Figure 10(b) shows the calculated band structure of pristine 2ML MoS_2; it is an indirect band gap material with the valence-band maximum at Γ high-symmetry point in the Brillouin zone (BZ), and the conduction-band minimum at K. We use (red) arrows to depict the indirect band gap, $E_g(\Gamma_v, K_c)$, the direct band gap, $E_g(K_v, K_c)$, and the difference between the top of the valence band at Γ and K points of BZ, $\Delta E(\Gamma_v, K_v)$.

We test how different values of parameters τ, n_{exp}, r_c, and n_c in Eq. (B2) influence $E_g(\Gamma_v, K_c)$, $E_g(K_v, K_c)$, and $\Delta E(\Gamma_v, K_v)$; five fiducial distance scaling parameter sets, $f(r_0, r)$, are given in Table I.

Figure 10(c) shows how $E_g(\Gamma_v, K_c)$, $E_g(K_v, K_c)$, and $\Delta E_g(\Gamma_v, K_v)$ vary with the distance between MLs, $c/2$. Specifically, with the increase of the distance between MLs (i) the indirect band gap increases almost linearly; with the increase in c by $\sim$2 Å, $E_g(\Gamma_v, K_c)$ increases by $\sim$237–330 meV, depending on $f(r_0, r)$ (Table I). For example, for $\Delta c = 2.05$Å, $\Delta E_g(\Gamma_v, K_c) = 238$ meV with $f_1(r_0, r)$, and $\Delta E_g(\Gamma_v, K_c) = 328$ meV with $f_2(r_0, r)$.

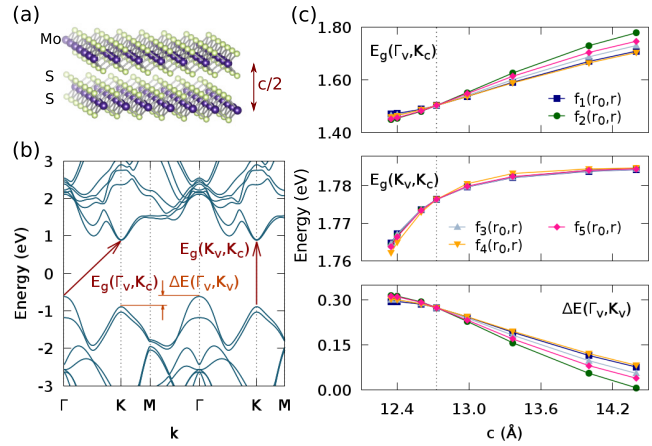

FIG. 10. (a) Structure of pristine 2ML MoS_2, where c is the lattice parameter perpendicular to the plane of the structure determining the distance between two MLs; (b) calculated band structure of 2ML MoS_2, where arrows depict the indirect band gap $E_g(\Gamma_v, K_c)$, the direct band gap $E_g(K_v, K_c)$, and the difference between the top of the valence band at Γ and K points, $\Delta E(\Gamma_v, k_v)$; (c) variation of $E_g(\Gamma_v, K_c)$, $E_g(K_v, K_c)$, and $\Delta E(\Gamma_v, k_v)$ with the lattice parameter c. The dotted line denotes the value of $c = 2.729$ eV used in the initial fitting of the TB parameter set, see Refs. [24,74,75].

(ii) The direct band gap, $E_g(K_v, K_c)$ also increases, but for $\Delta c = 2.05$Å, $\Delta E_g(K_v, K_c)$ increases by $\sim$20 meV; for example, for $\Delta c = 2.05$Å, $\Delta E_g(K_v, K_c) = 19.6$ meV with $f_1(r_0, r)$, and $\Delta E_g(K_v, K_c) = 22.7$ meV with $f_4(r_0, r)$.

(iii) $\Delta E(\Gamma_v, K_v)$ reduces. The largest drop is found for $f_2(r_0, r)$ distance scaling parameter set, where for $c = 14.4$ Å and $\Delta E_g(\Gamma_v, K_v) = 6.5$ meV. As a precaution when choosing suitable parameters, we note that for a fixed c and a certain combination of parameters, it is possible to artificially shift top of the valence band at Γ point down and make a 2ML MoS_2 a direct K_v-K_c band-gap material. We have eliminated those nonphysical scenarios from the analysis.

As it can be seen in Fig. 10(c), the variation of $E_g(\Gamma_v, K_c)$, $E_g(K_v, K_c)$, and $\Delta E(\Gamma_v, k_v)$ with the distance between MLs *is not qualitatively influenced* by the choice of the distance scaling parameter set, Table I. The reported differences for here considered $f(r_0, r)$ are only quantitative, where the direct band gap $E_g(K_v, K_c)$ is the least sensitive to the choice of a parameter set from Table I.

TABLE I. Parameters in Eq. (B2) for the distance scaling of hopping and overlap integrals.

param.	orb.	$f_1(r_0, r)$	$f_2(r_0, r)$	$f_3(r_0, r)$	$f_4(r_0, r)$	$f_5(r_0, r)$
τ	s-s	2.0	2.0	2.0	2.0	2.0
	s-p	2.0	2.0	2.0	2.0	2.0
	p-p	2.0	2.0	2.0	2.0	2.0
	p-d	3.5	3.5	3.5	2.0	3.5
	d-d	5.0	5.0	5.0	2.0	5.0
n_{exp}	*all*	0.0	$=\tau$	$=\tau$	$=\tau$	0.25
r_c	*all*	–	2.5	3.5	3.5	1.5
n_c	*all*	–	4.0	4.0	4.0	2.0

TABLE II. Distance scaling for nearest neighbor NN, (within a ML) and van der Waals, vdW, type (second nearest-neighbor S-S) interactions for the nanoplatelet [Fig. 8(a) left panel and nanostructured bilayer [Fig. 8(a) right panel]; $f_1(r, r_0)$ and $f_1(r, r_0)$ are defined in Table I and Eq. (B2). Calculated Fermi energies for nano and nanostructured bilayer MoS_2 systems depending on the choice of the distance scaling are given in the last two columns. Note that for the MoS_2 nanoplatelet there is no influence of vdW type interactions, thus only distance scaling of NN interactions is relevant.

Dist. scal.	NN	vdW	$E_f^{(\text{nano})}$ (eV)	$E_f^{(\text{hybrid})}$ (eV)
f_1^{nano}	$f_1(r_0, r)$	$f_1(r_0, r)$	−0.8782	−0.8744
f_2^{nano}	$f_3(r_0, r)$	$f_3(r_0, r)$	−0.8779	−0.8757
f_3^{nano}	$f_1(r_0, r)$	$f_3(r_0, r)$	−0.8782	−0.8758

Our results *agree qualitatively* with DFT predictions [94,95]. For example, Zhou *et al.* employed DFT method with generalized gradient approximation as parametrized by Perdew, Burke, and Ernzerhof, and reported that by the increase in c by 2 Å (from 12.4 to 14.4Å) results in the increase of the indirect band gap by $\Delta E_g(\Gamma_v, K_c) = 310$ meV, and the direct band gap by $\Delta E_g(K_v, K_c) = 30$ meV [94]. Although results extracted from DFT are sensitive to the adopted exchange-correlation functional and particular implementation [8,94], we see that our TB findings [Fig. 10(c)] are in a good agreement with the predictions of Zhou *et al.* [94]

Next, we discuss how different parameter sets in our distance scaling constant [Eqs. (B1) and (B2)], influence the electronic properties of nanoplatelets and nanostructured bilayer systems, investigated in the main body of the manuscript. To analyze the distance scaling constant we employ the same nanoplatelet and nanostructured bilayer system shown in Fig. 8(a), and calculate DOS for those systems.

In our analysis, we distinguish between the nearest-neighbor interactions (NN), relevant for both our model nanoplatelet and nanostructured bilayer, and vdW type interactions, relevant only for our model nanostructured bilayer. We analyze a wide range of parameters for the distance scaling constant, and the three distinct cases are shown in Table II. First one, f_1^{nano}, assumes that the distance scalings for NN and vdW interactions obey the Harrison universal form [81,93], the second one f_2^{nano} assumes that the distance scaling both, for NN and vdW, includes exponential decay, using parameters of $f_3(r_0, r)$ defined in Table I. The third f_3^{nano} distinguishes between NN interactions, which were modeled assuming the Harrison universal form, and the vdW interactions, modeled using the exponential decay. As a reminder to the reader, we note there is no vdW interactions for nanoplatelets, only the distance scaling for NN is relevant.

Figure 11 shows calculated DOS for the relaxed nanoplatelet and nanostructured bilayer MoS_2 materials using the scaling constants given in Table II. We see that the different parameter sets in the scaling constant do not influence DOS and do not cause any qualitative changes. Also, focusing on the Fermi energies (last two columns in Table II), we see that different scaling constants from Table II introduce only minor variations, less than 1.5 meV. In the main body of the manuscript, we show results using the parameter set of the scaling constant f_3^{nano}.

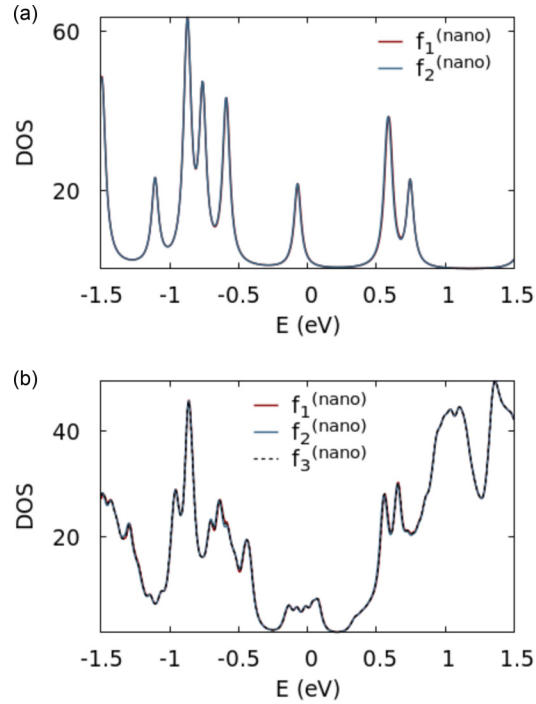

FIG. 11. Calculated DOS for the relaxed MoS_2 nanoplatelet (a) and nanostructured bilayer (b) for different distance scaling constants. The structures of the model nanoplatelet and nanostructured bilayer are shown in Fig. 8(a), and parameter sets for the distance scaling constants in Table II.

APPENDIX C

Technical details regarding the calculations of DOS, pDOS, and Re[σ]) are given in Ref. [24]. Here, we present basic explanations.

DOS is defined as

$$D(E) = \sum_{\mathbf{k},n} \delta(E - \epsilon_{\mathbf{k},n}), \tag{C1}$$

Partial DOS of an orbital α in the atom b is given by

$$D_{b\alpha}(E) = \sum_{\mathbf{k},n} \delta(E - \epsilon_{\mathbf{k},n}) C^{\dagger}_{\mathbf{k},n}(b,\alpha) S(\mathbf{k}) C_{\mathbf{k},n}(b,\alpha). \tag{C2}$$

We remind the reader that for any two band indexes n and m: $C^{\dagger}_{\mathbf{k},n} S(\mathbf{k}) C_{\mathbf{k},m} = \delta_{nm}$. For solving Eqs. (C1) and (C2), instead of Dirac delta function, we assume Lorentzian-broadening function, with typically broadening of $\Gamma = 30$ meV.

Optical response of our nanostructured bilayers is obtained from the calculated real part of optical conductivity in the dipole approximation [8,24,62–67]:

$$\text{Re}[\sigma(\omega)] = \frac{\pi e^2}{2\hbar\omega m_e^2} \sum_{n}^{\text{occ}} \sum_{m}^{\text{empty}} \int_{1BZ} \frac{d^3\mathbf{k}}{(2\pi)^2} |p_{nm}(\mathbf{k})|^2 \delta \times (\epsilon_{m,\mathbf{k}} - \epsilon_{n,\mathbf{k}} - \hbar\omega), \tag{C3}$$

where $\hbar\omega$ is the photon energy, p_{nm} is the momentum matrix element, and ϵ_n and ϵ_m are converged eigenenergies of nth and mth bands, respectively. Also, e denotes the electron charge and m_e the electron mass. The integration is carried over the

first Brillouin zone (1BZ). For more details regarding Eq. (C3) see, e.g., Refs. [8,63].

In the case of TB method [24,64,65], the momentum matrix element p_{nm} is calculated directly from the TB (or SCTB) Hamiltonian and the expansion coefficients for the eigenvectors, without additional parameters:

$$p_{nm}(\mathbf{k}) = \sum_{b\alpha,b'\alpha'} = C^{\dagger}_{\mathbf{k},n}(b,\alpha)C_{\mathbf{k},m}(b',\alpha') \times \sum_{\mathbf{R}} e^{i\mathbf{k}\mathbf{R}}\mathbf{R}E^{bb'}_{\alpha\alpha'}(\mathbf{R}), \tag{C4}$$

where $E^{bb'}_{\alpha\alpha'}(\mathbf{R})$ is the Slater-Koster matrix of tight-binding parameters [76], defined using our input TB parameter set [73,74]. As was the case for DOS calculations, in solving Eq. (C3), instead of Dirac delta function we employ Lorentzian-broadening function.

As also mentioned in the main body of the manuscript, for calculating the real part of optical conductivity in Eq. (C3) we consider only interband transitions. There is, however an additional contribution to the optical conductivity, coming from intraband transitions. Because momentum conservation is not satisfied for direct absorption of a photon by an intraband optical transition [63]. These transitions depend on lattice imperfections (and temperature); and are often represented using phenomenological expression [24,63]: $\mathrm{Re}[\sigma^{\mathrm{intra}}(\omega)] = \sigma_0/(1+\omega^2\tau_D^2)$, where σ_0 and τ_D denote dc conductivity and the electron scattering time, respectively. Discussion regarding this issue can be found in our Ref. [24]. For transition energies discussed in this work, these transitions can be neglected [24,63,68–70].

[1] K. F. Mak, C. Lee, J. Hone, J. Shan, and T. F. Heinz, Phys. Rev. Lett. **105**, 136805 (2010).
[2] F. Cadiz, E. Courtade, C. Robert, G. Wang, Y. Shen, H. Cai, T. Taniguchi, K. Watanabe, H. Carrere, D. Lagarde, M. Manca, T. Amand, P. Renucci, S. Tongay, X. Marie, and B. Urbaszek, Phys. Rev. X **7**, 021026 (2017).
[3] L. Yuan, T.-F. Chung, A. Kuc, Y. Wan, Y. Xu, Y. P. Chen, T. Heine, and L. Huang, Sci. Adv. **4**, e1700324 (2018).
[4] P. Schmidt, F. Vialla, S. Latini, M. Massicotte, K.-J. Tielrooij, S. Mastel, G. Navickaite, M. Danovich, D. A. Ruiz-Tijerina, C. Yelgel, V. Fal'ko, K. S. Thygesen, R. Hillenbrand, and F. H. L. Koppens, Nat. Nanotechnol. **13**, 1035 (2018).
[5] Q. H. Wang, K. Kalantar-Zadeh, A. Kis, J. N. Coleman, and M. S. Strano, Nat. Nanotechnol. **7**, 699 (2012).
[6] T. Cao, G. Wang, W. Han, H. Ye, C. Zhu, J. Shi, Q. Niu, P. Tan, E. Wang, B. Liu, and J. Feng, Nat. Commun. **3**, 887 (2012).
[7] T. C. Berkelbach and D. R. Reichman, Annu. Rev. Condens. Matter Phys. **9**, 379 (2018).
[8] M. Gibertini, F. M. D. Pellegrino, N. Marzari, and M. Polini, Phys. Rev. B **90**, 245411 (2014).
[9] M. Bernardi, M. Palummo, and J. C. Grossman, Nano Lett. **13**, 3664 (2013).
[10] W. Bao, X. Cai, D. Kim, K. Sridhara, and M. S. Fuhrer, Appl. Phys. Lett. **102**, 042104 (2013).
[11] S. Kim, A. Konar, W.-S. Hwang, J. H. Lee, J. Lee, J. Yang, C. Jung, H. Kim, J.-B. Yoo, J.-Y. Choi, Y. W. Jin, S. Y. Lee, D. Jena, W. Choi, and K. Kim, Nat. Commun. **3**, 1011 (2012).
[12] B. Radisavljevic, A. Radenovic, J. Brivio, V. Giacometti, and A. Kis, Nat. Nanotechnol. **6**, 147 (2011).
[13] P. Rivera, K. L. Seyler, H. Yu, J. R. Schaibley, J. Yan, D. G. Mandrus, W. Yao, and X. Xu, Science **351**, 688 (2016).
[14] Y. Li, J. Ludwig, T. Low, A. Chernikov, X. Cui, G. Arefe, Y. D. Kim, A. M. van der Zande, A. Rigosi, H. M. Hill, S. H. Kim, J. Hone, Z. Li, D. Smirnov, and T. F. Heinz, Phys. Rev. Lett. **113**, 266804 (2014).
[15] T. Cai, S. A. Yang, X. Li, F. Zhang, J. Shi, W. Yao, and Q. Niu, Phys. Rev. B **88**, 115140 (2013).
[16] A. Chaudhari, T. Ghoshal, M. T. Shaw, J. O'Connell, R. A. Kelly, C. Glynn, C. O'Dwyer, J. D. Holmes, and M. A. Morris, Adv. Mater. Interf. **3**, 1500596 (2016).
[17] G. Li, D. Zhang, Q. Qiao, Y. Yu, D. Peterson, A. Zafar, R. Kumar, S. Curtarolo, F. Hunte, S. Shannon, Y. Zhu, W. Yang, and L. Cao, J. Am. Chem. Soc. **138**, 16632 (2016).
[18] E. V. Calman, C. J. Dorow, M. M. Fogler, L. V. Butov, S. Hu, A. Mishchenko, and A. K. Geim, Appl. Phys. Lett. **108**, 101901 (2016).
[19] K.-A. Min, J. Park, R. M. Wallace, K. Cho, and S. Hong, 2D Mater. **4**, 015019 (2017).
[20] M. V. Bollinger, J. V. Lauritsen, K. W. Jacobsen, J. K. Nørskov, S. Helveg, and F. Besenbacher, Phys. Rev. Lett. **87**, 196803 (2001).
[21] P. Cui, J.-H. Choi, W. Chen, J. Zeng, C.-K. Shih, Z. Li, and Z. Zhang, Nano Lett. **17**, 1097 (2017).
[22] S. Helveg, J. V. Lauritsen, E. Lægsgaard, I. Stensgaard, J. K. Nørskov, B. S. Clausen, H. Topsøe, and F. Besenbacher, Phys. Rev. Lett. **84**, 951 (2000).
[23] T. Li and G. Galli, J. Chem. Phys. C **111**, 16192 (2007).
[24] V. Mlinar, Phys. Chem. Chem. Phys. **19**, 15891 (2017).
[25] Y. Gong, J. Lin, X. Wang, G. Shi, S. Lei, Z. Lin, X. Zou, G. Ye, R. Vajtai, B. I. Yakobson, H. Terrones, M. Terrones, B. K. Tay, J. Lou, S. T. Pantelides, Z. Liu, W. Zhou, and P. M. Ajayan, Nat. Mater. **13**, 1135 (2014).
[26] Y. Gong, S. Lei, G. Ye, B. Li, Y. He, K. Keyshar, X. Zhang, Q. Wang, J. Lou, Z. Liu, R. Vajtai, W. Zhou, and P. M. Ajayan, Nano Lett. **15**, 6135 (2015).
[27] V. Mlinar, Phys. Rev. B **96**, 235437 (2017).
[28] H. Terrones, F. López-Urías, and M. Terrones, Sci. Rep. **3**, 1549 (2013).
[29] Y. Li, Y. Rao, K. F. Mak, Y. You, S. Wang, C. R. Dean, and T. F. Heinz, Nano Lett. **13**, 3329 (2013).
[30] X. Su, R. Zhang, C. Guo, M. Guo, and Z. Ren, Phys. Chem. Chem. Phys. **16**, 1393 (2014).
[31] K. Kośmider and J. Fernández-Rossier, Phys. Rev. B **87**, 075451 (2013).
[32] S. Yuan, R. Roldán, M. I. Katsnelson, and F. Guinea, Phys. Rev. B **90**, 041402(R) (2014).
[33] S. Salehi and A. Saffarzadeh, Surf. Sci. **651**, 215 (2016).
[34] A. Ramasubramaniam, D. Naveh, and E. Towe, Phys. Rev. B **84**, 205325 (2011).

[35] W. Li, T. Wang, X. Dai, X. Wang, C. Zhai, Y. Ma, S. Chang, and Y. Tang, Solid State Commun. **250**, 9 (2017).

[36] C. Zhao, T. Norden, P. Zhang, P. Zhao, Y. Cheng, F. Sun, J. P. Parry, P. Taheri, J. Wang, Y. Yang, T. Scrace, K. Kang, S. Yang, G.-X. Miao, R. Sabirianov, G. Kioseoglou, W. Huang, A. Petrou, and H. Zeng, Nat. Nanotechnol. **12**, 757 (2017).

[37] F. Rose, M. O. Goerbig, and F. Piéchon, Phys. Rev. B **88**, 125438 (2013).

[38] A. Srivastava, M. Sidler, A. V. Allain, D. S. Lembke, A. Kis, and A. Imamoglu, Nat. Phys. **11**, 141 (2015).

[39] G. Aivazian, Z. Gong, A. M. Jones, R.-L. Chu, J. Yan, D. G. Mandrus, C. Zhang, D. Cobden, W. Yao, and X. Xu, Nat. Phys. **11**, 148 (2015).

[40] D. MacNeill, C. Heikes, K. F. Mak, Z. Anderson, A. Kormányos, V. Zólyomi, J. Park, and D. C. Ralph, Phys. Rev. Lett. **114**, 037401 (2015).

[41] V. Mlinar, J. Phys.: Condens. Matter **30**, 275502 (2018).

[42] A. F. Rigosi, H. M. Hill, Y. Li, A. Chernikov, and T. F. Heinz, Nano Lett. **15**, 5033 (2015).

[43] L. Kou, T. Frauenheim, and C. Chen, J. Phys. Chem. Lett. **4**, 1730 (2013).

[44] J. Kang, S. Tongay, J. Zhou, J. Li, and J. Wu, Appl. Phys. Lett. **102**, 012111 (2013).

[45] D. Saha and S. Mahapatra, Appl. Phys. Lett. **108**, 253106 (2016).

[46] J. D. Cain, E. D. Hanson, and V. P. Dravid, J. Appl. Phys. **123**, 204304 (2018).

[47] J. Kunstmann, T. B. Wendumu, and G. Seifert, Phys. Status Solidi (b) **254**, 1600645 (2017).

[48] H. Wang, C. Zhang, and F. Rana, Nano Lett. **15**, 339 (2015).

[49] H. Wang, J. H. Strait, C. Zhang, W. Chan, C. Manolatou, S. Tiwari, and F. Rana, Phys. Rev. B **91**, 165411 (2015).

[50] J. P. Lauritsen, J. Kibsgaard, S. Helveg, H. Topsoe, B. S. Clausen, E. Lægsgaard, and F. Besenbacher, Nat. Nanotechnol. **2**, 53 (2007).

[51] Y. Xue, Y. Zhang, Y. Liu, H. Liu, J. Song, J. Sophia, J. Liu, Z. Xu, Q. Xu, Z. Wang, J. Zheng, Y. Liu, S. Li, and Q. Bao, ACS Nano **10**, 573 (2016).

[52] H.-J. Kim, Y.-W. Song, S. D. Namgung, M.-K. Song, S. Yang, and J.-Y. Kwon, Opt. Lett. **43**, 4590 (2018).

[53] M. Tripathi, A. Mittelberger, N. A. Pike, C. Mangler, J. C. Meyer, M. J. Verstraete, J. Kotakoski, and T. Susi, Nano Lett. **18**, 5319 (2018).

[54] H. Ye, J. Zhou, D. Er, C. C. Price, Z. Yu, Y. Liu, J. Lowengrub, J. Lou, Z. Liu, and V. B. Shenoy, ACS Nano **11**, 12780 (2017).

[55] Y.-C. Lin, O. D. Dumcenco, Y.-S. Huang, and K. Suenaga, Nat. Nanotechnol. **9**, 391 (2014).

[56] V. Mlinar, Nanotechnology **24**, 042001 (2013).

[57] V. Mlinar, Ann. Phys. (Berlin) **527**, 187 (2015).

[58] C. Barreteau, D. Spanjaard, and M. C. Desjonquères, Phys. Rev. B **58**, 9721 (1998).

[59] Y. Xie, and J. A. Blackman, Phys. Rev. B **64**, 195115 (2001).

[60] M. Xia, B. Li, K. Yin, G. Capellini, G. Niu, Y. Gong, W. Zhou, P. M. Ajayan, and Y-H. Xie, ACS Nano **9**, 12246 (2015).

[61] S. J. Jenkins, Phys. Rev. B **70**, 245401 (2004).

[62] C. S. Wang, and J. Callaway, Phys. Rev. B **9**, 4897 (1974).

[63] H. Ebert, Rep. Prog. Phys. **59**, 1665 (1996).

[64] L. C. Lew Yan Voon, and L. R. Ram-Mohan, Phys. Rev. B **47**, 15500 (1993).

[65] B. Jogai, Solid State Commun. **116**, 153 (2000).

[66] D. L. Dexter, Solid State Phys. **6**, 353 (1958).

[67] F. Trani, G. Cantele, D. Ninno, and G. Iadonisi, Phys. Rev. B **72**, 075423 (2005).

[68] I. V. Solovyev, Phys. Met. Metallogr. **91**, S199 (2001).

[69] E. G. Maksimov, I. I. Mazin, S. N. Rashkeev, and Y. A. Uspenski, J. Phys. F: Met. Phys. **18**, 833 (1988).

[70] J. L. Erskine, and E. A. Stern, Phys. Rev. B **8**, 1239 (1973).

[71] D. J. Chadi, Phys. Rev. B **16**, 790 (1977).

[72] R. Roldán, M. P. López-Sancho, F. Guinea, E. Cappelluti, J. A. Silva-Guillén, and P. Ordejón, 2D Mater. **1**, 034003 (2014).

[73] F. Zahid (private communication).

[74] F. Zahid, L. Liu, Y. Zhu, J. Wang, and H. Guo, AIP Adv. **3**, 052111 (2013).

[75] L. Liu, and F. Zahid (unpublished).

[76] J. C. Slater, and G. F. Koster, Phys. Rev. **94**, 1498 (1954).

[77] V. Mlinar, J. Mater. Chem. **22**, 1724 (2012).

[78] P. Koskinen, and V. Mäkinen, Comp. Mater. Sci. **47**, 237 (2009).

[79] We demonstrated a reasonable agreement between the electronic structure extracted from our parametrized TB method and those from DFT calculations for the case of relatively large MoS_2-based nanowires and nanoplatelets [24,27].

[80] G. Hegde, M. Povolotskyi, T. Kubis, T. Boykin, and G. Klimeck, J. Appl. Phys. **115**, 123703 (2014).

[81] W. A. Harrison, *Electronic Structure and the Properties of Solids* (Freeman, San Francisco, 1980).

[82] W. A. Harrison, Phys. Rev. B **31**, 2121 (1985).

[83] G. K. Straub, and W. A. Harrison, Phys. Rev. B **31**, 7668 (1985).

[84] J. A. Majewski, and P. Vogl, Phys. Rev. B **35**, 9666 (1987).

[85] C. M. Goringe, D. R. Bowler, and E. Hernández, Rep. Prog. Phys. **60**, 1447 (1997).

[86] R. S. Mulliken, J. Chem. Phys. **23**, 1833 (1955).

[87] R. S. Mulliken, J. Chem. Phys. **3**, 573 (1935).

[88] D. D. Johnson, Phys. Rev. B **38**, 12807 (1988).

[89] D. Vanderbilt, and S. G. Louie, Phys. Rev. B **30**, 6118 (1984).

[90] G. P. Srivastava, J. Phys. A-Math. Gen. **17**, L317 (1984).

[91] S. Froyen, and W. A. Harrison, Phys. Rev. B **20**, 2420 (1979).

[92] L. Goodwin, A. J. Skinner, and D. G. Pettifor, Europhys. Lett. **9**, 701 (1989).

[93] J. Zhao, Y. Luo, and G. Wang, Eur. Phys. J. D **14**, 309 (2001).

[94] W. Zhou, C. Yuan, A. Hong, X. Luo, and W. Lei, Nanoscale **10**, 1145 (2018).

[95] C. Espejo, T. Rangel, A. H. Romero, X. Gonze, and G.-M. Rignanese, Phys. Rev. B **87**, 245114 (2013).

[96] V. Mlinar, J. Phys.: Conf. Ser. **939**, 012015 (2017).

[97] X. Zhang, F. Zhang, Y. Wang, D. S. Schulman, T. Zhang, A. Bansal, N. Alem, S. Das, V. H. Crespi, M. Terrones, and J. M. Redwing, ACS Nano **13**, 3341 (2019).

[98] F. Zhang, Y. Wang, C. Erb, K. Wang, P. Moradifar, V. H. Crespi, and N. Alem, Phys. Rev. B **99**, 155430 (2019).